ION BEAM MIXING OF Mo/Al BILAYER SAMPLES AND THERMAL SPIKE EFFECTS

by

Geng-Sheng Chen

thesis submitted to the Faculty of the

Virginia Polytechnic Institute and State University

in partial fulfillment of the requirements for the degree of

Master of Science

in

Materials Engineering

APPROVED:

Diana Farkas, Chairperson

Charles R. Houska

Jack L. Lytton

November, 1987

Blacksburg, Virginia

ION BEAM MIXING OF Mo/Al BILAYER SAMPLES AND THERMAL SPIKE EFFECTS

by

Geng-Sheng Chen

Diana Farkas, Chairperson

Materials Engineering

(ABSTRACT)

Metallic bilayer samples of Mo(400 Å)/Al(substrate) were characterized using Rutherford Backscattering Spectroscopy after first being irradiated with Xe ion beam having an energy of 1.8 MeV. The computer code RUMP was then used to simulate the RBS spectra. The interdiffusion at the interface was considered in terms of thermal spike induced atomic migration. It was found that the coupling of the chemical effect with spike is significant with regard to mixing of the bilayer samples. Furthermore, in addition to the initial contamination of carbon atoms on the surface and at the interface, more carbon atoms were found to be picked up by the surface, this carbon was from the vacuum pumps and tended to migrate into the surface once irradiation dose exceeded $11 \times 10^{15}/cm^2$.

A semi-empirical model was developed for ion beam mixing taking into account collisional mixing and thermal spike effects, as well as the thermal spike shape. The collisional mixing part was accounted for by the Kinchin-Pease model, or, alternatively dynamic Monte Carlo simulation. For the thermal spike, the ion beam mixing parameter Dt/Φ was derived to be proportional to $(-F_D/\Delta H_{coh})^{2+\mu}$, where F_D is the damage energy deposited per unit path length, ΔH_{coh} is the cohesive energy of the target materials, and μ is a constant dependent on the spike shape and point defect density in the spike regions. The thermal spike introduces a nonlinear effect in the mixing process, distinguishing itself from the linear effect of ballistic mixing. The shape of the thermal spike that best fit the experimental results depends on the magnitude of the cascade density. For relatively high density collisional cascades, where thermal spikes start to be important, it was found that a spherical spike model was more consistent with experimental measurements at low temperatures. However, for ex-

tremely high density collisional cascade regions, a cylindrical shaped spike gave better results.

The atomic migration energy in the spike regions is scaled by a factor of one out of 8.6 of cohesive energy. The migration mechanism was recognized to be interstitial-dominated one.

Acknowledgements

The author owes the deep gratitude to his advisor, Dr. Diana Farkas, for her valuable guidance and stimulating encouragement during completion of this work. Thanks are also due to Dr. C. R. Houska for his cooperation and encouragement, and Dr. J. L. Lytton for his participation as a committee member throughout the program.

Grateful appreciation is due to Mr. M. Rangaswamy for both his assistance and fruitful discussions. Thanks also go to the author's fellow graduate students for their assistance and camaraderie throughout the study. Furthermore, many thanks to Ms Karen Macleod and Dr. M. O. Lewus who spent a lot of time unselfishly attempting to polish the final version of this thesis.

The author is greatly indebted to Dr. Graham Hubler and Dr. Ken Grabowski, of the Naval Research Laboratory, for providing useful experimental details and for helpful discussions. He acknowledges Mr. Roberto C. Pasianot, of the Atomic Energy Commission, Argentina, for his computer simulation code TRALL co-created with Mr. M. Rangaswamy.

Finally, the author wishes to express his thanks to Ms Zheng Wu in encouraging his study mentally, and to his parents, who have missed their son on the other side of the Pacific Ocean.

The author wish to acknowledge L. R. Doolittle for providing the computer program RUMP to analyze the RBS data.

Financial support by the Office of Naval Research under Contract # N00014-85--K-0110 is gratefully acknowledged.

Table of Contents

List of Illustrations

List of Tables

1.0 INTRODUCTION

1.1 Applications of Ion Beam Mixing Techniques

Ion beam mixing is a unique method of modifying and fabricating advanced materials and devices, and in recent years has been used in an increasing number of applications. This has stimulated the interest of many researchers and has caused an increase in the number of studies in this area. Common area of application includes: (1) Microelectronics, (2) Surface and vacuum technology, (3) Synthesis of artificial materials from the multilayer targets, (4) Materials characterization by ion sputtering. An understanding of the mechanism of ion beam mixing is necessary in order to optimize ion beam mixing methods in these areas of application. In addition, the interesting phenomena which occur during the ion mixing process offer new information concerning the interaction between charged particles and solids, as well as defect-induced effects in the cascade damage region etc. Knowledge of Solid-State Physics and Materials Science is involved in explanations of the experimental results.

1.2 Ion Mixing Aspects

Averback[1] outlined the different aspects of ion beam mixing at both low and high temperatures. Computer modelling of ion beam mixing by the Monte Carlo method has been carried out in dealing with the binary collisional mixing, and also molecular dynamics simulation has been used in the many body interactions. It has been recognized that ballistic mixing, thermal spike induce diffusion, chemically driven migration, and radiation-enhanced diffusion, are distinct mechanisms which play significantly roles during ion beam mixing. Two different stages have been recognized during ion beam mixing process, and has been termed the prompt region and the delayed region by Johnson [2].

Another comprehensive investigation has been carried out by Pain and Averback [3]. They surveyed the experimental work concerning ion mixing of marker layer systems and bilayer systems carried out in the last few years. Ballistic mixing was recognized as having a significant effect on ion beam mixing, but other mechanisms, e.g., thermal spike, also play an important role under certain mixing conditions. In fact, consideration of ballistic mixing alone is not enough to explain a lot of tabulated experimental results even if the displacement energy E_d in the ballistic mixing modelling is adjusted. The changing of E_d can not alter the result of mixing by a factor of 2. As an example of this kind of discrepancy, it was determined that the average mixing efficiencies were greater than the collisional mixing theory by factors of 13 and 110 for the marker layer mixing in matrices of Si and Ge respectively [3]. This result can not be accounted for even by the most sophisticated collisional mixing model developed by Sigmund [4]. Pain and Averback[3] also concluded that the advantage of the elimination of a chemical effect in ion mixing of marker layer systems can fail to occur, at least for many semiconductor systems. On the other hand, since no correlation exists between the mixing efficiencies of different marker layers and their heat of mixing, Kim et al [5] concluded from their experiments on metallic marker layer mixing by use of ion beam that there was no sign of existence of a chemical effect.

It should be emphasized that the importance of marker layer ion beam mixing rests on the testing of the degree of ion mixing of bulk materials. Fenn-Tye and Marwick[6] conducted ion beam mixing of metallic marker layer Pd(200 Å)/Pt(5 Å)/Pd systems using different incident energetic ions at low temperatures. Their results showed that the mixing efficiency was a step-like variation when the mixing efficiency was plotted against the energy deposited per unit path length. This means that different mechanisms become dominant as F_D. increases. In fact as the author developed in the following parts, their results come from thermal spike related nonlinear effects in the high cascade region. Similar experimental work of marker layer mixing by ion beam was also carried out by Bottiger et al [7] with a marker layer sample of Ni(400 Å)/Au(10 Å)/Ni. The nonlinear effect of the deposited energy per unit path length on the mixing efficiency clearly exists, however, a quantitative description is difficult to derive due to the large deviation in the experimental results.

As early as 1974, Andersen and Bay[8] found out from their sputtering experiments involving use of a Au target, that the nonlinear effect caused by heavy-ion implantation is accompanied with the mixing process. Unfortunately, the collisional mixing model is not able to account for their result. In other work carried out by Thompson and Walker [9], the defects generated in a cascade volume was studied experimentally by subjecting Si and Ge targets to heavy-ion bombardment respectively. A semi-empirical formula was developed for describing the density of defects created in the high cascade regions of the two targets respectively. There are two components in the formula, one is the energy spike related defects in the high cascade regions, the second is the defects created by the collisional process. The result indicates that the existence of nonlinear effects originates from many-body interactions of atoms in the liquid-like regions. This will be discussed more in Chapter 5.

In other work done by Kim et al [10], an investigation of the ion beam mixing of metallic markers in matrices of Cu and beta-Zr was conducted. It was found that the impurity mechanisms for atomic migration in the thermal spike regions could be important. In the Cu matrices, the migration of marker species occurs as a result of a substitutional mechanism, however, in beta-Zr matrices, it is either substitutional or interstitial.

1.3 Other Relevant Work

Rapid migration of marker layer in certain elemental matrices have been found by many research groups. The marker layers of Au and Pt in polycrystalline Al matrices were subject to ion beam irradiations in work carried out by Barcz and Nicolet [11]. It was found that the rapid migration of Au and Pt inside Al matrices is similar to grain boundary diffusion. Similar results were also observed in the migration of Carbon through TiFe alloys [12] and this was considered to be due to chemical effects in this systems. Computer modelling of these experiments have been carried out successfully [13].

Tao et al. [20] conducted twin marker layer ion beam mixing experiments. From this work relative shifting was found after RBS data of the as-deposited samples and irradiated samples were analyzed. A comparison was then made between ion beam mixing and thermal annealing. It was found that an inverse-Kirkindall effect occurred in the damage regions, and that effect played an important role during mixing.

Rao and Houska et al [22,23] used an X-ray technique to characterize the defect forms in irradiated samples. The samples they analyzed were Nb and Mo films which had been subjected to N irradiation at two different temperatures. It was found that the implanted N atoms were in the form of a single defect at low temperatures. This suggested that the ion beam mixing for this specific case has nothing to do with the long range relaxation of point defects since these point defects are immobile at low temperatures. In addition, it is not feasible in this case to rule out atomic migration in the short-term range, the phenomenon being induced by the spike in the damage regions. This is consistent with the assumption made by Peak [28]. On the other hand, defect-cluster formation at relative high temperatures demonstrates that the radiation-enhanced diffusion starts to play an important role in the atomic migration process in the damage regions.

Summary:

(1) Mixing mechanisms, excluding collisional mixing mechanism, are responsible for the atomic transport processes which occur during ion beam mixing.

(2) The existence of nonlinear effect of damage deposited energy on the mixing efficiency is beyond what the ballistic mixing model can predicted.

(3) The rapid migration of impurity atoms through some host media is similar to a grain boundary mechanism. This may alternatively be accounted for by a chemical assisted migration mechanism.

(4) The damaged volume may produce some new phenomena, which can be different from those suggested by traditional theory, e.g., the energy damage gradient can generate an inverse-Kirkindall effect.

(5) Defects were found to be of either single or cluster types and these vary under different experimental conditions.

2.0 REVIEW

2.1 Ion Mixing Mechanisms

2.1.1 Ballistic Mixing

The atomic transport of recoiled atoms and the subsequent series of cascade collisions constitute the ballistic mixing effect. Extensive theoretical studies have been done by Winterbon [29], Sigmund [4], and Anderson [34]. Ballistic mixing was found to have a diffusion-like process and this can be expressed in an analytical way. If the cascade mixing process is considered to be near ideal random mixing, and the atomic diffusion is taken to occur in an elemental cubic volume with isotropic randomness, then the effective diffusion coefficient for ballistic mixing can be expressed as:

$$D_b = \frac{1}{6} r_c^2 P \qquad (2-1)$$

where

r_c = the root-mean square jumping distance and related to the ballistic mixing process; It is also defined r_t as the root-mean square jumping distance relevant to thermal spike induced migration, different from r_c,

P = the number of displacements per target atom per unit time.

P can be expressed by

$$P = \frac{0.42\ \Phi\ F_D}{\rho\ \ t\ \ E_d} \qquad (2-2)$$

where

Φ = the incident ion dosage

t = the irradiation time

ρ = the atomic density of the target ($Å^{-3}$)

Thus the mixing parameter obtained is

$$L_b \equiv \frac{D_b t}{\Phi} = \frac{0.42}{6\rho} F_D \frac{r_c^2}{E_d} \qquad (2-3)$$

The mixing parameter L_b is independent of time and temperature in the ballistic mixing process. Experimental work has been carried out involving the ion beam mixing efficiency L_b in different temperature ranges in the bilayer of Nb/Si and Cr/Si systems [37]. It was found that the mixing efficiency is weakly dependent on the temperature below certain critical temperature points. Therefore the ballistic mixing was suggested for some time to be the dominating mechanism in the ion beam mixing process. However, the experimental results are always much greater than the ballistic mixing prediction even after using adjusted

values of some parameters, such as E_d is about 30 eV, r_c is several lattice constants. Sufficient experiments have carried out to suggest that thermal spike induced diffusion also plays an important role during heavy bombardment of high energetic incident ions (E > 100 KeV) penetrating a heavy target (Z > 20). In fact thermal spike induced diffusion can also be temperature-independent, and this will be discussed further in Chapter 5.

2.1.2 Thermal Spike

The high density collisional cascade generates a lot of displaced atoms in a very localized volume. While these atoms cannot displace other atoms further, they can impart some of their energy to neighboring atoms through a many-body interaction. Thus most of their neighbor atoms are thermalized or energetically equalized in accordance to the Boltzmann-Maxwell distribution, and this results in a liquid-like spike region in which the average characteristic energy of each atom is around 1 eV. This corresponds to a temperature of the order of ten thousand K. The spike dimension is around 100 angstroms, i.e., ten lattice constants [9]. So localized volume and so much difference in temperature with the bulk, the spike will quench rapidly that the spike region becomes metastable or even amorphous state. Normally the spike time last from 10^{-13} s to 10^{-10} s.

Vineyard developed a phenomenological model which assumes that the spike shape is cylinder-like. The initial condition of the spike is an energetic line described by the damage energy density $F_D\delta^2(r)$, where

$$T(r, 0\_) = 0 \qquad (2-4)$$

and

$$T(r, 0_+) = \frac{F_D}{c}\delta^2(r) \qquad (2-5)$$

where

r is the radical distance from the initial energetic line.

c is the specific heat of the target material.

$\delta^2(r)$ is the two dimension delta-function.

The initial bulk target temperature is simply taken to be zero since at low temperatures radiation enhanced diffusion is suppressed, and the mixing efficiency is only weakly dependent on temperature. Assuming that the heat conduction coefficient κ and specific heat capacity c are temperature-independent constants, for isotropic and chemically homogeneous media the heat conduction equation is given by

$$\kappa\Delta T(r, t) = c\frac{\partial T(r, t)}{\partial t} \qquad (2-6)$$

The infinite boundary condition is

$$T(r, t)|_{r\to\infty} = 0 \qquad (2-7)$$

The solution to the above equation is

$$T(r, t) = \frac{F_D}{4\pi\kappa t}e^{-\frac{cr^2}{4\kappa t}} \qquad (2-8)$$

Assume the number of thermally activated jumps per unit volume per unit time is given by

$$Ae^{-Q/T}$$

where

A is temperature-independent constant,

Q is the defect thermal migration energy, and also is temperature-independent

Then the total number of thermally induced jumps in one spike per unit length of spike η_c, isgiven by

$$\eta_c = \int_0^\infty 2\pi r dr \int_0^\infty A e^{-\frac{Q}{T(r,t)}} dt \qquad (2-9)$$

Using

$$x = \frac{cr^2}{4\kappa t}$$

instead of the integral variable r, we can then solve the integral easily, namely

$$\eta_c = \frac{AF_D^2}{8\pi\kappa c Q^2} \qquad (2-10)$$

In the next chapter Vineyard's idea will be followed, with the spike shape and thermally activated defects covered in more details since some of the most recent experiments make this improvement directly comparable with.

2.1.3 Thermochemical Effect

Johnson et al [2] studied the thermochemical influence on the ion beam mixing process. They combined the Vineyard cylindrical spike model with consideration of chemically biased random walking, and this modified model was expressed by multiplying the effective jumps with the Darken term $(1 - 2\Delta H_m/T)$, where ΔH_m is the heat of mixing of the target materials. Thus, a phenomenological model of chemical effects coupled with the en-

ergy spike was reached in a qualitative way. Therefore, the previous consideration in the Vineyard model, the total number of jumps for one spike per unit length of the spike were calculated after modifying the number of jumps per unit volume per unit time into the form of

$$Ae^{-Q/T}(1-2\frac{\Delta H_m}{T})$$

i.e.,

$$\eta_c = \int_0^\infty 2\pi r dr \int_0^\infty Ae^{-Q/T}(1-2\frac{\Delta H_m}{T})dt \qquad (2-11)$$

the integral can be completed as in the previous case, see equation (2-9)

$$\eta_c = \frac{AF_D^2}{8\pi\kappa cQ^2}(1-4\frac{\Delta H_m}{Q}) \qquad (2-12)$$

The total number of jumps in the spike region, after being irradiated up to the dose Φ, can be expressed by $\eta_c\Phi/\rho$, where ρ is the atomic density of the target material ($Å^{-3}$). The typical jumping distance r_1 can be related to ρ by

$$r_1 = q_1\rho^{-1/3}$$

The cohesive energy of the material is equal to the energy difference between free atom and the atom in the crystal position. The cohesive energies of pure elements can be found out from ref. [19]. The activation energy, Q, should be scaled by the cohesive energy, i.e.,

$$Q = -q_2\Delta H_{coh}$$

Here q_1 and q_2 are positive constants. Eventually the chemically aided spike induced mixing can be expressed as

$$\frac{D_T^c t}{\Phi} = \frac{K_1 F_D^2}{\rho^{5/3}(\Delta H_{coh})^2}(1 + K_2 \frac{\Delta H_m}{\Delta H_{coh}}) \qquad (2-13)$$

where

K_1 can be considered approximately constant and is dependent on κ, c, and A;

K_2 is a constant related to q_2.

The experimental work [16] which was first published in 1984, demonstrates the good consistency with later developed phenomenological model [14]. Equation (2-13) was derived in Y. T. Cheng et al's paper [14].

2.2 Numerical Methods in Ion Mixing Modelling

Two ion beam mixing mechanisms have been described using analytical and numerical techniques. The first is the collisional process of mixing: binary collision process in ballistic simulation and molecular dynamics simulation in many-body involved collisional process. The second deals with the thermal spike induced diffusion mechanism in which a partial relaxation of defects occurs in the high cascade volume.

2.2.1 Collisional Cascade Induced Atomic Transport

The damage energy deposited per unit path length, F_D, is one of the most useful parameters in the characterization of the ion beam mixing process. The Monte Carlo computer simulation code TRIM reported in 1980 [24] is the commonly accepted program for an-

alyzing recoil collisions and collisional cascade processes, and offers a way of calculating a value for F_D. Though the assumptions made in TRIM, such as, the amorphous target, the selected value of sublimation energy and displacement energy, are not very suitable for specific simulation cases, they do not influence the final obtained damage energy distribution since these parameters do not play such a significant role in the high density cascade region. TRIM gives the damage energy profile as one of the outputs.

The computer code TRALL[27] is modified from TRIM and is used for obtaining the concentration profile induced by ballistic mixing. The accuracy of the program itself depends on the number of particles simulated and the dose step of each run of the program.

2.2.2 Energy Spike Induced Atomic Migration

By considering the energy spike as a locally hot zone, Peak and Averback[28] attempted to use a numerical technique to analyze the thermally activated atomic diffusion process. In their modelling, a spherical hot zone is assumed, and its radius is obtained from the mean straggling and transverse straggling parameters given by Winterbon[29]. Vacancies created in the collisional process are distributed uniformly in the sphere spot, the number of these point defects is calculated from the modified Kinchin-Pease formula [30]. The results of this analyses suggest that the of thermal spike has a significant effect in ion beam mixing. Unfortunately this analyses are not suitable for characterizing the explicit formulation of the mixing efficiency with certain descriptive parameters of the target materials, such as the cohesive energy, the heat of mixing, and the damage energy deposited in the cascade regions.

The Vineyard model[32] simplified the mathematical model by making some assumptions (see in the following sections). Though some of the assumptions seems too simple, such as the delta-function approximation for the initial condition of the heat conducting equation, this model serves as approach of keeping the general trends. It is a good

semi-quantitative model on certain aspects. However, the point defect density, as an important factor, is not considered in the model. This makes the Vineyard model inadequate to be used for practical analyses.

2.3 Damage Regions in Collision Process

2.3.1 Damage Energy Distribution

The damage energy is characterized by the damage energy line density, i.e., the energy deposited by elastic collisions per unit path length. Basically F_D depends on four parameters determined by the target material, namely, atomic density, atomic number, atomic mass, and displacement energy of the target material. The computer simulation code TRIM [24] provides a method of obtaining the energy damage parameter, F_D. For bilayer systems, however, the damage energy distribution can have a sharp change at the interface in the case of ideal bilayer samples, depending on the four parameters of the bilayer elements as mentioned above. The way it is used to obtain the damage energy line density at the interface is as follows:

$$F_D = [\frac{1}{11} \sum_{i=-5}^{5} F_D^2(x_i)]^{1/2} \qquad (2-14)$$

where the average is determined over eleven points in the vicinity of the interface of the bilayer system, that is, in a range of 100 Å to 200 Å normal to the interface. The eleven points $F_D(x_i)$ $(i = -5, -4, -3, ..., +5)$ are the deposited energy at each point of x_i with depth interval ($x_i - x_{i-1}$) from 10 Å to 40 Å. Equation (2-14) is a good approximation which can be used to

calculate F_D in most cases where the bilayer samples are subjected to the ion beam irradiation. The energy damage gradient, however, can induce an extra effect as described in the previous section. This makes the mixing analysis more complicated. Fortunately this effect is not significant and can be neglected for most of the studies which have been carried out to date.

2.3.2 Cascade Shapes and Sizes

When the energy spikes are considered to have a dominant effect on the ion beam mixing process, the cascade shapes and sizes become a considerable influencing factor in the mixing mechanism study since they are involved in setting up the boundary conditions and initial conditions of the spike temperature for the heat conduction equation. For example, in the Vineyard spike model [32] or Peak and Averback [28] numerical calculation of spike induced diffusion, the spike was assumed to be cylindrical and spherical respectively in the models used. The main difference of this result rests on the fact that for different spike shape, the mixing parameter will have different dependence on the damage energy deposited.

Heinisch [33] has studied the high energy collisional cascade by computer simulation, and in his studies cascade shapes and sizes in Fcc metals were displayed for particles with two different energies penetrating a metallic target. It was found that when the incident energy of the particle is greater than a certain value, the overlapping of cascades along the sub-tract of recoiled atoms will be so large that closely-spaced cascades chains are formed, i.e., a cascade shape transition occurs from an isolated compact one to closely linked chains. This is an interesting result when compared with the thermal spike analysis to be developed later in the present work (see Chapter 4 and Chapter 5).

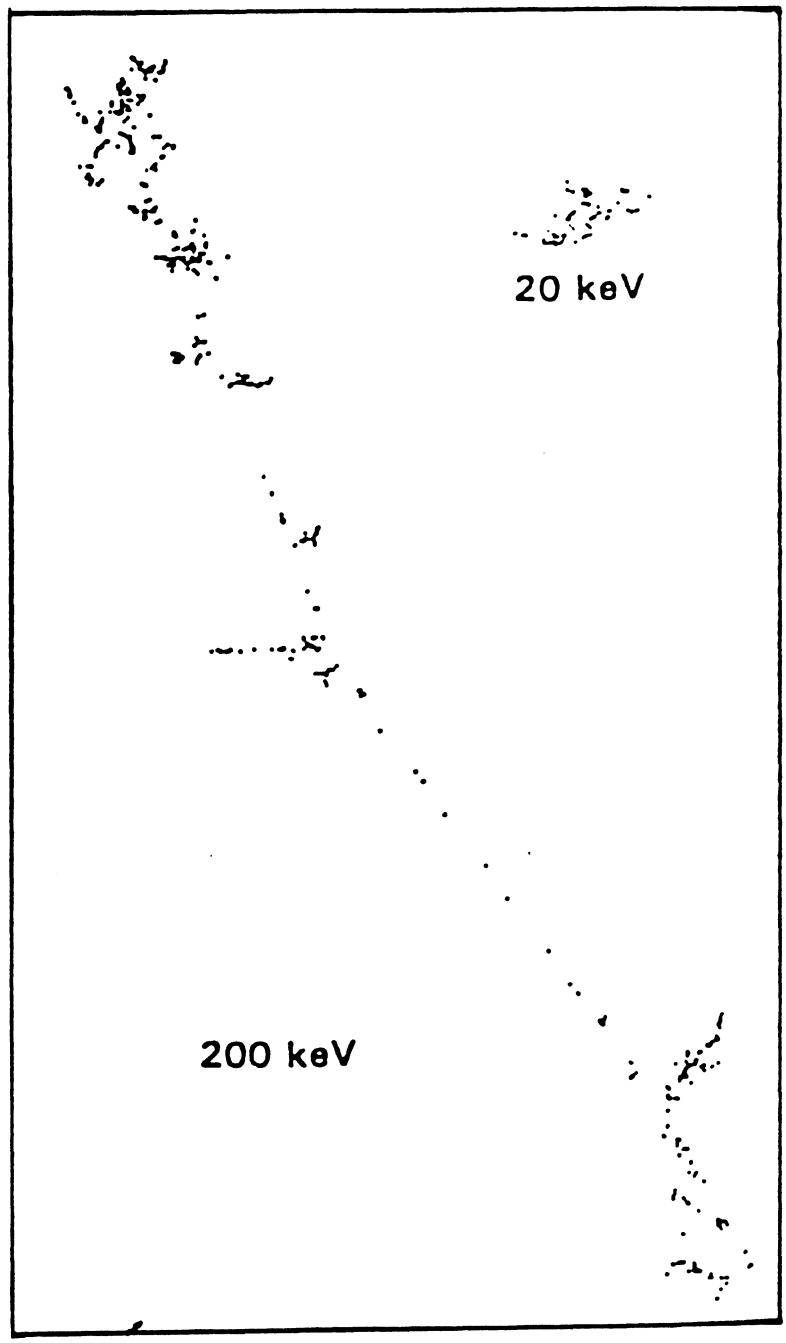

Figure 1. Simulation of vacancy distribution following recombination, the incident energies are 20 KeV and 200 keV. The length of this cascade is 278 lattice parameters (100 nm) [33].

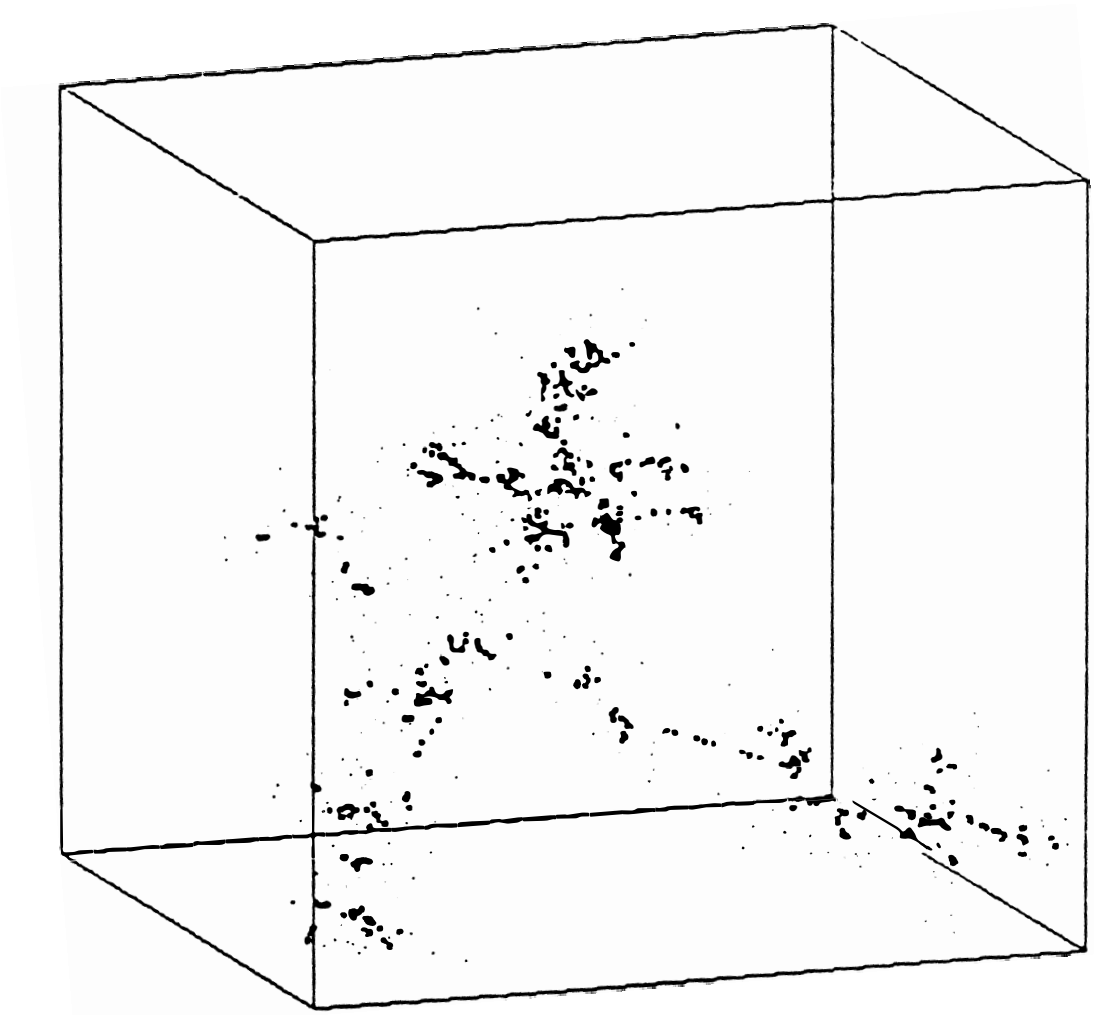

Figure 2. Distribution of vacancies and interstitial after subsequent recombination. The incident energy is 200 KeV. The cube side is 125 lattice parameters (45 nm) [33].

2.3.3 Atomic Displacement Caused by Collision Cascade

After the collisional process ends, a very high density of point defects are created in the cascade region. Since many interstitials lie within the recombination volumes of nearby vacancies, (defect pairs separated distance normally is of several lattice parameters), these Frenkel pairs then recombine with each other spontaneously, i.e., immediately after the cascade collisions end. Finally the number of point defects is reduced to a number of displaced atoms N, and this number can be predicted by Kinchin-Pease formula [30]

$$N = \frac{0.42E_D}{E_d} \qquad (2-15)$$

where

E_D = the damage energy.

E_d = the displacement energy of the target atom. This value is taken to be 13 eV to 30 eV in most of the published results involving ballistic mixing.

These defects play an important role during the spike induced diffusion process. As a binary collisional approximation the Kinchin-Pease model is suitable for low and relatively high density cascade regions. In the case of extremely high density cascade regions, the spike region becomes liquid-like, and the binary-interaction model may no longer be valid. Molecular dynamics, an analytical tool used to treat many-body interactions in the collisional mixing process, holds the promise as a mean of describing the ion beam mixing in solids.

Displaced atoms in the cascade region was also studied experimentally and semi-theoretically by Thompson and Walker[9]. A semi-empirical formulation was developed for energy spike induced defects in the cascade regions of silicon and germanium, semiconductor materials. They proposed that the defects generated by high-Z bombardment is comprised of two components, namely, the defects created in the collisional cascade process,

and the defects induced by the energy spike. The following semi-empirical formulation was then obtained for the number of defects created in the cascade region:

$$N_D = K(1 - e^{-F_D\lambda/\nu}) + N \qquad (2-16)$$

where

K is a constant, which corresponds to the saturation number of defects induced by the energy spike.

ν is an energy related constant.

λ is the characteristic dimension of collisional cascade volume.

The term $F_D\lambda$ is the damage energy in a characteristic cascade volume. The two constants in this model, namely, K and ν, are variables related to materials with different physical properties. This makes the semi-quantitative analysis of ion beam mixing process complicated if the Thompson-Walker model is used.

2.3.4 Fractal-Geometry Approach

A number of problems have links with the idea of fractal geometry. As example, this approach has been used in the studying of natural framework of the coastline geometry, disorder materials, and galaxy formation. The idea might also be of interest in atomic collisions in solids. The fractal-geometry approach in the studies of cascades and spikes was recently employed by Y. T. Cheng [38]. Figure 4 shows the two-dimension fractal trees which demonstrates the idealized collisional framework. The collisional cascade and the subsequent spike are characterized well in this way. The results obtained correlate to those worked out with some other ways. Since this approach seems to be able to display a clear physical picture of collisional cascade and its relationship with the subsequent spike, it appears that

the method holds promise for providing an insight into the cascade phenomenon and spike effects. However, the information obtained in this way is a result of statistical averages. Consequently, it can only show the general trends, and as a result some other aspects related to the target-material properties are lost.

2.4 *Experimental Work*

2.4.1 Marker Layer Mixing Experiments

Marker layer samples are composed of a thin elemental layer (around 10 Å or even less) embedded in a matrix, which is otherwise a homogeneous, isotropic material. In the case of a marker layer inserted into a metallic matrix, the marker layer region can be regarded as a dilute solid solution in which any chemical effects can be neglected in the ion beam mixing process. The elimination of chemical effects is an advantage in the marker layer system, since unlike the bilayer system, as mentioned in the previous section, the chemically biased diffusion may dominate.

Rutherford Backscattering spectroscopy (RBS) is normally used to determine the broadening of the marker layer profile. Since the RBS signals of the marker layer are Gaussian-like before and after the irradiations, the broadening of the Gaussian-like damage energy profile, due to ion beam mixing, is measured from the signals yielded by both irradiated (Ω^2_{irr}) and unirradiated samples (Ω^2_{unirr}), i.e.,

$$\Omega^2 = \Omega^2_{irr} - \Omega^2_{unirr} \qquad (2-17)$$

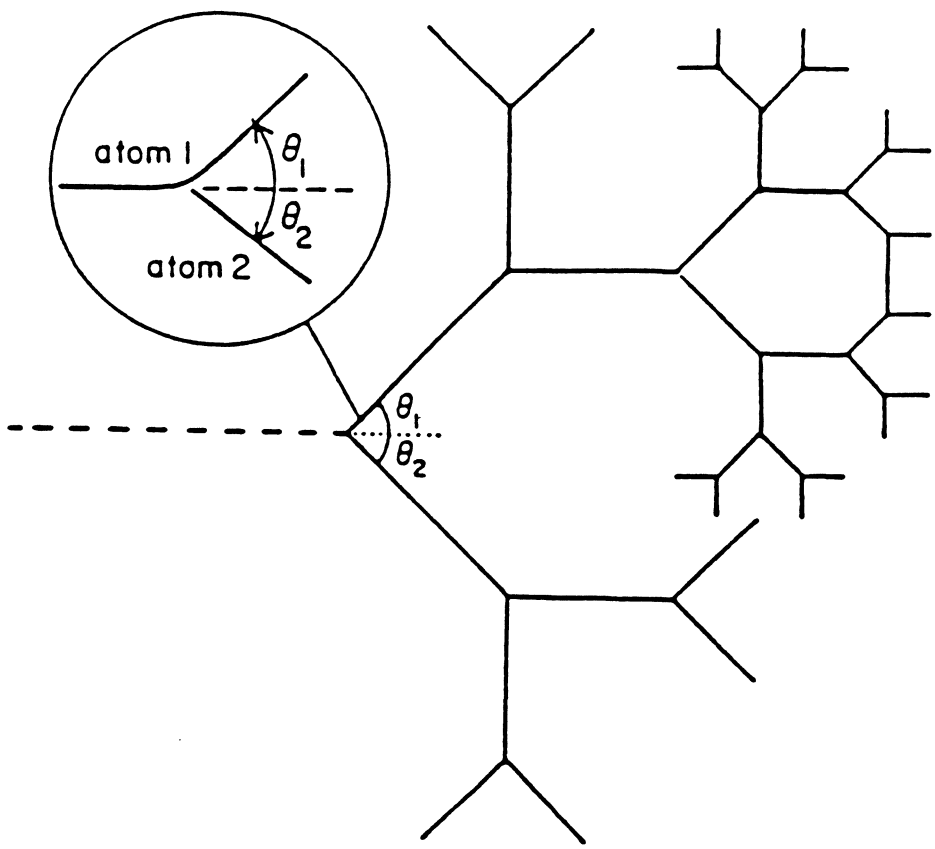

Figure 3. Fractal tree for analyzing an idealized collisional cascade [38].

where

Ω_{irr} is the yields of RBS signals after being subjected to ion mixing,

Ω_{unirr} is the yields of RBS signals for as-deposited samples.

Then the standard deviation of the marker layer profile, σ , can be calculated from

$$\sigma = \Omega / N_0 \varepsilon \qquad (2-18)$$

where

N_0 is the atomic number density of the target material (cm^{-3}),

ε is the stopping cross-section factor which He ions are back scattered by the marker layer atoms embedded in matrices.

Now that the parameter has been determined, the effective diffusion length Dt can be easily obtained, i.e.,

$$Dt = \varepsilon^2 / 2$$

2.4.2 Bilayer Mixing

Bilayer samples are directly related to the materials surface modification problems. They are fabricated by depositing one layer onto a substrate followed by deposition of the second layer. The top layer thickness is normally 200 Å to 500 Å, depending on what degree of energetic damage is preferred. Since the interdiffusion of a bilayer is also governed by chemical driving forces, the coupling of the chemical effect with thermal spikes may provide a way of investigating the chemical biased diffusion effect.

RBS is generally employed in the determination of the concentration profile. The computer simulation code RUMP provides a powerful analytical way of determining the con-

centration profile, and it is very sensitive to the energy spectrum when the bilayer elements have high mass ($Z > 20$), and the difference in mass between the bilayer elements are large. Finally the concentration profile can be analyzed using the Boltzmann-Matano method for the interdiffusion case. Then the approximate effective diffusion parameter, Dt, can be obtained from an error-function least square fitting. The small departures from the erfc-shape are a result of either the chemically biased interdiffusion or the large energy damage gradient at the interfaces [20]. This will be considered in the following section.

Recently, a series of ion beam mixing experiments using metallic bilayer samples were carried out at Cal Tech [15,16,17]. Their experimental work showed that thermochemical effects play an important role in bilayer mixing cases involving both heavy incident ions and heavy metal matrix ($Z > 20$) atoms, especially for systems with a large chemical characteristic parameter $\Delta H_m/\Delta H_{coh}$, where ΔH_{coh} is the cohesive energy of the target materials, ΔH_m is the heat of mixing. The latter was obtained in work by Miedema 18], and it can be approximated for binary alloys of 1-1 composition at the interface of bilayer samples. The cohesive energy of the binary alloys $A_{50}B_{50}$ is then calculated from

$$\Delta H_{coh} = \frac{1}{2}(\Delta H_A^0 + \Delta H_B^0) + \Delta H_m \qquad (2-19)$$

where

ΔH_A^0 is the cohesive energy corresponding to element A,

ΔH_B^0 is the cohesive energy corresponding to element B [19].

2.4.3 The Effect of Energy Damage Gradient

Experimental evidence has revealed that the damage energy gradient at the interfaces of metal-semiconductor, metal-metal and semiconductor-semiconductor bilayer systems, is attributable to movement of certain species as a consequence of being subjected to

high dose ion implantation [20]. In the experiments carried out by Tao et al [20], a twin marker layer sample of Ge(1160Å)/W(5Å)/Mg(1770Å)/W(5Å)/Ge(substrate) was irradiated by 360 Kev Ar^+. The Rutherford backscattering spectra revealed that the relative shift between the twin marker layers of W was caused by the damage energy gradient, since the damage energy in the Mg layer region is greater than than that of Ge. The atomic transport from the low damage region to the high damage region is analogous to the inverse Kirkendall effect observed in the interdiffusion experiment of some of the metallic systems.

It should be emphasized here that the chemically biased diffusion at the interface also plays an important role in the species W shifting of twin marker layer sample when being subjected to the high dose ion implantation. If the ion implantation damage-controlled migration is in the same direction of the thermochemical induced interface shifting, the total shifting of the marker layer will be increased, otherwise the total shift will be decreased.

It is pertainal to mention that the influence of the steady state defect profile might be more important than the instantaneous damage profile calculated by the computer simulation code TRIM. If the binding energy between metal atom and vacancy is small, then the metal atom will be easier to move and this may result in position exchange with the semiconductor elements.

2.5 *Temperature Influences on Ion Mixing*

Ion beam mixing process is temperature-dependent. Two distinguished mixing mechanisms exist at different temperature regions. At low temperatures, below a certain value Tc, a number of recent experiments [36,37] have demonstrated that the mixing efficiency has only a weak temperature-dependence. Figure 4 is the bilayer Cr(200 Å)/Si(substrate) [37] which was subjected to 45 KeV Cr ion irradiation, and the mixing result was plotted for the mixing efficiency with temperature. Normally, the critical temperature T_c is around the room

temperature for metal-semiconductor systems, and may be as low as the liquid nitrogen temperature for metallic systems.

At high temperatures (above the critical point) the radiation enhanced diffusion dominates and increases rapidly with the temperature. Here the research focuses on ion beam mixing study at low temperatures in which the radiation enhanced diffusion is suppressed.

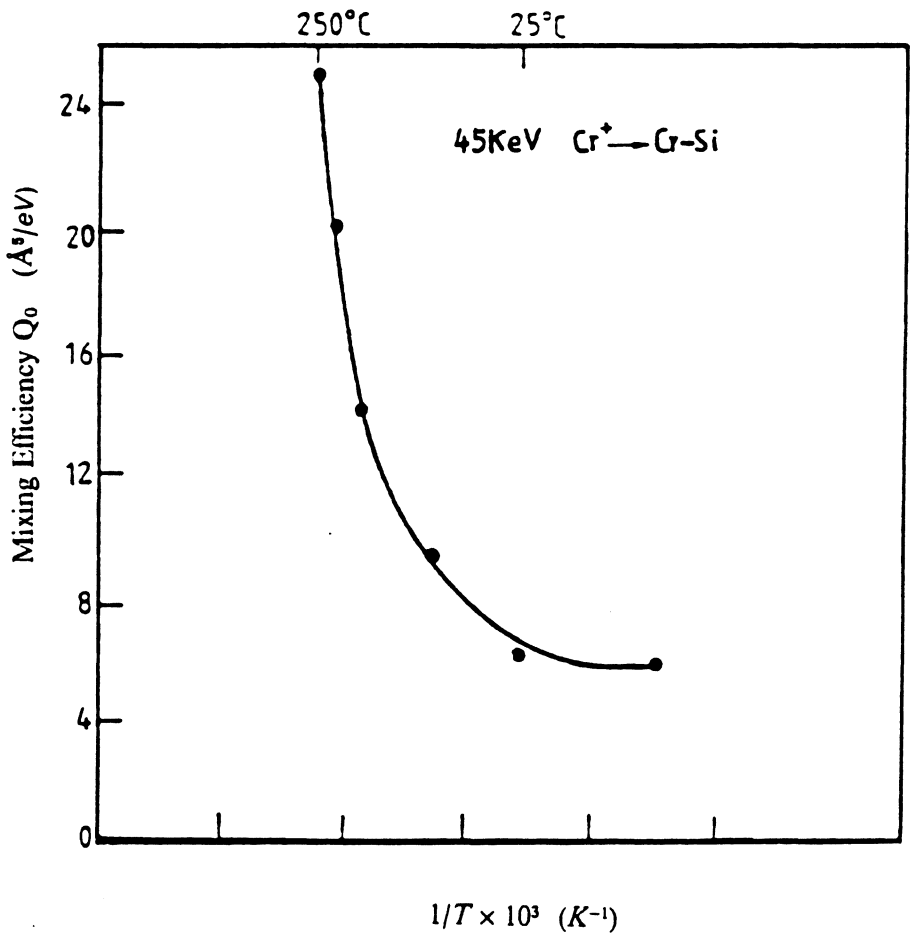

Figure 4. The ion beam mixing efficiency of Cr/Si bilayer samples under different temperatures [37].

3.0 Ion Beam Mixing of Mo-Al Bilayer Systems

3.1 Introduction

Rutherford backscattering spectroscopy (RBS) is a frequently used technique in ion beam mixing analyses. As an analytical method, the RBS technique involves light-bombardment (usually H^+, He^+, or He^{++}) but at very high energy (0.5 MeV to 3.0 MeV). The energy spectrum in RBS is the energy distribution of the backscattered projectile ions. The attainable composition profile can be up to 1μm, depending on the energy of the incident ion beam.

As the incident ion passes through the target material it loses energy to the outer-shell electrons of the target atoms. The sensitivity of the RBS technique depends on the atomic mass of impurity elements and the atomic mass of the matrix elements in which the impurity element is embedded. High mass impurity element in a low mass matrix would exhibit higher sensitivity. However, the sensitivity is poor to resolve light mass elements with atomic weigh close to or less than 10 a.m.μ. Furthermore, the RBS technique is suitable for metallic bilayer systems in which two metallic elements are well separated in atomic mass. The Mo/Al bilayer system is ideal in this respect of considerations.

3.2 The Computer Code RUMP

The computer code RUMP is a software package obtained from Cornell University. It was developed by Larry Doolittle and Mike Thompson [40,41]. The program RUMP was used to analyze the RBS data presented in this thesis.

RUMP basically provides a means of simulating the RBS spectra in an iterative way. The composition profile can be obtained automatically when the compositions of each layer are set up, and the spectrum relevant to this profile is then compared with an experimental spectra. These steps are followed continuously until a desired fitting matches up almost completely with the experimental spectra. RUMP can generate spectra for both H and He atom beams or their respective ion beams, and claims to be able to produce recoil spectra as well. It includes its own tables containing isotopic abundances, masses, and elemental density. The package also allows for Bohr straggling, pulse pileup, nonuniform thick layers, and interdiffusion of bilayers. Spectral files on the VAX are read into RUMP where a header is attached to them. The header contains the experimental parameters to be used for data acquisition. Default values are assigned by RUMP, but they can easily be changed by the user. As an example, the scattering factor has a default value which is set up by RUMP, but it is readily altered in the SIM mode. RUMP can also provide considerable interactive manipulation and interpretation of RBS spectra. For example, elemental edge positions are easily identified by using the cursor.

Two papers were reported [40,41] on the different fundamental aspects which are the basis of RUMP. The outline described in these publications makes us aware of what we are operating while doing the simulation routine.

3.3 Description of Experimental Work

The metallic bilayer samples Mo/Al were fabricated at Naval Research Laboratory (NRL). These samples were Al disks on top of which Mo films having a thickness of about 400 Å were deposited. They were then intermittently subjected to Xe ion beam irradiation having an energy of 1.8 MeV. The irradiation dose ranged from $1 \times 10^{15}/cm^2$ to $4.02 \times 10^{16}/cm^2$. RBS analyses were done with 1.8 MeV He^+, without breaking vacuum. The runs were performed over two days. Energy calibration standards were run on both days. The parameter CONVERS used for ADC calibration were 3.879 and 10.551. The sample tilt angle THETA was 37 (sometimes -22.5). The beam to detector angle PHI was 45. The detector solid angle Omega was 1.33. The detailed description for each of the specific analyzed spectrum is attached to each of the figures of the following pages. The obtained composition profiles are shown on the next pages of each of the figures.

In order to correct the nominal charge values to account for analyzer dead time, the CORRECT factor in RUMP was used instead of correcting the nominal charge values directly. The reason for doing this lies in the fact that the charge acquisition in this case seemed to be out of way.

3.4 Analyses

All of the RBS data recommended for analyses have been characterized by using RUMP. The data are classified in three groups. Group no. one includes the as-deposited samples for the calibration of RBS analyses. Group no. two are the samples subjected to relative low doses ($1 \times 10^{15}/cm^2$ to $17 \times 10^{15}/cm^2$) of Xe ion irradiations. Group no. three in-

cludes the samples subjected to high dose ($30.2 \times 10^{15}/cm^2$ to $40.2 \times 10^{15}/cm^2$) irradiations. The following lists the files that each of the classified Groups include.

Group no. 1 files: run104 and run133 (Al disk), run105 and run130 (Mo standard film), run103 (as-deposited Mo/Al sample).

Group no. 2 files: run107 and run108 (irradiated with dose of $1 \times 10^{15}/cm^2$), run110 (irradiated with dose of $3 \times 10^{15}/cm^2$), run113 (irradiated with dose of $7 \times 10^{15}/cm^2$), run118 (irradiated with dose of $11 \times 10^{15}/cm^2$), run120 (irradiated with dose of $17 \times 10^{15}/cm^2$).

Group no. 3 files: run127 (irradiated with dose of $30.2 \times 10^{15}/cm^2$), run129 (irradiated with dose of $40.2 \times 10^{15}/cm^2$).

In Group no. one, the Al disk (run104 and run133) which was used as the substrate for the bilayer Mo/Al samples, was found to contain a high concentration of oxygen within the top layer of 100 Å. This is due to the formation of Al_2O_3 once the pure Al disk is exposed to the air. In contrast, the Mo films had a tendency to pick up carbon atoms within the top layer of 100 Å. However, the migrating ability of carbon atoms within the Mo film is higher than that of oxygen into the Al disk. While the Al_2O_3 layer on the top of the Al disk acts as a strong diffusion barrier and prevents the diffusion of oxygen atoms, the Mo-C layer on the top of Mo film does not provide such an effective barrier and carbon atoms can still diffuse into the material.

Figure 8 shows the as-deposited sample. In order to fit the Al-edge part, carbon atoms must be taken into account at the interface of Mo/Al bilayer samples. The reason for this is due to the fact that carbon atoms are easily picked up on the top of Al disk once the first few layers of Mo atoms are deposited layer by layer onto the Al disk in the vacuum. Inside the Mo film, well away from the surface and interface, no carbon was detected. This tendency for carbon pick-up at the Mo/Al interface and on the Mo film surface is often found when metallic films are fabricated by deposition in vacuum. Since RBS is not sensitive to light-mass atoms, such as carbon, so the carbon atom profiles in the analyses presented in this thesis

are not very accurate. Nevertheless, the RBS characterization of the carbon profiles does illustrate general trends and are therefore of considerable use.

For the samples irradiated with relatively low doses ($1 \times 10^{15}/cm^2$ to $17 \times 10^{15}/cm^2$), the interfaces of Mo/Al were increasingly mixed with increasing the doses. As the dose reached a value of $\simeq 11 \times 10^{15}/cm^2$, the carbon atoms absorbed on the surface of the Mo film tended to migrate inwards. This was indicated by the appearance of the inward region of the spectra corresponding to the Mo edge. In the dose range of $11 \times 10^{15}/cm^2$ to $17 \times 10^{15}/cm^2$, the concentration of carbon atoms on the surface increased with the irradiation dose.

As the irradiation dose is increased even more ($30.2 \times 10^{15}/cm^2$ to $40.2 \times 10^{15}/cm^2$), the fitting became more complicated since more and more Xe atoms remain inside the samples. In other word, the neglecting of the presence of Xe atoms is no longer valid, however, but the general trends can still give the right information. As shown in the table 9 and table 10, the amount of carbon atoms which migrated inside increased with the increase of doses. Some of Al atoms already reached the surface.

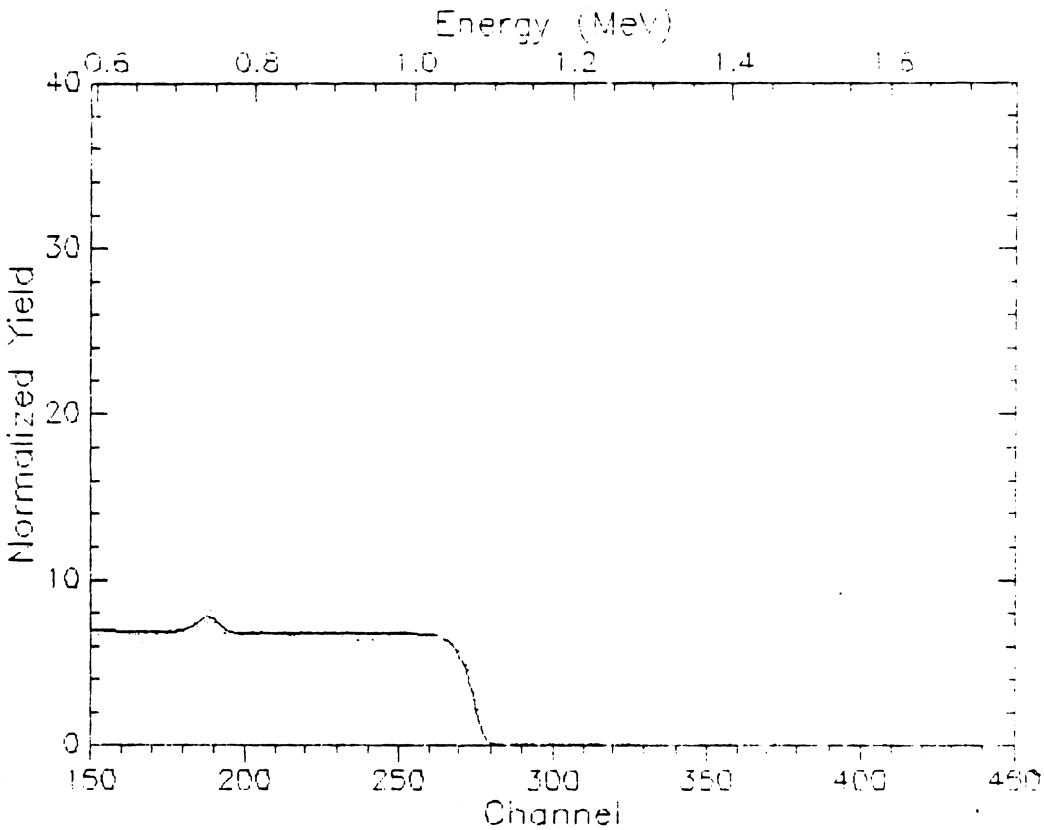


```
Current File: [RANGASW.SHENG]RUN104.RBS;1
Identifier:  Al disk as-deposited
Date:  September 18, 1987
1.800 MeV     40.00 uCoulombs
Channel Energy Constants:     3.8790     10.5510
Correction Factor:    0.9900
Angles (Theta, Phi, Omega):    37.0000     45.0000    1.330
Livetime text:
Channel number of first data point:     0.0
Number of data points:  513
Detector FWHM:      20.0 keV       Beam: He+
RMS Beam current:   50.0 nA    Geometry: IBM
```

Figure 5. Al disk (used as the substrate for the metallic bilayer Mo/Al).

Table 1. Al disk (used as the substrate for the metallic bilayer system of Mo/Al).

#	Thickness	Sublayers	Composition	. . .	
1	50.00 A	auto	Al 0.400	O	0.600
2	50.00 A	auto	Al 0.650	O	0.350
3	50.00 A	auto	Al 0.820	O	0.180
4	50.00 A	auto	Al 0.960	O	0.040
5	50.00 A	auto	Al 0.980	C	0.020
6	4000.00 A	auto	Al 1.000		

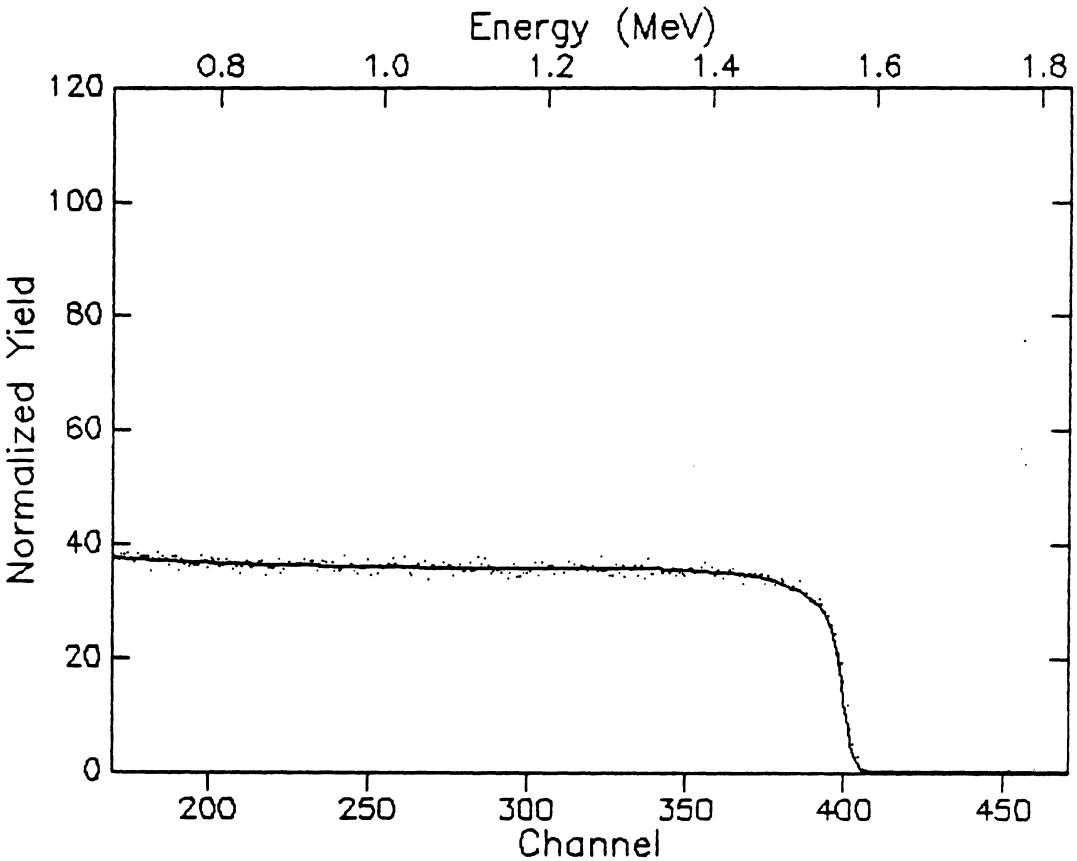


```
Current File: [RANGASW.SHENG]RUN130.RBS;1
Identifier:  Mo film as-deposited
Date:  September 18, 1987
1.800 MeV     10.00 uCoulombs
Channel Energy Constants:     3.8790     10.5510
Correction Factor:    0.9700
Angles (Theta, Phi, Omega):    37.0000     45.0000    1.330
Livetime text:
Channel number of first data point:     0.0
Number of data points:  513
Detector FWHM:      20.0 keV       Beam: He+
RMS Beam current:   50.0 nA    Geometry: IBM
```

Figure 6. Mo film as-deposited.

Table 2. Mo film as-deposited.

#	Thickness	Sublayers	Composition . . .			
1	50.00 A	auto	Mo	0.460	C	0.540
2	50.00 A	auto	Mo	0.600	C	0.400
3	50.00 A	auto	Mo	0.730	C	0.270
4	50.00 A	auto	Mo	0.820	C	0.180
5	50.00 A	auto	Mo	0.880	C	0.120
6	80.00 A	auto	Mo	0.920	C	0.080
7	80.00 A	auto	Mo	0.950	C	0.050
8	200.00 A	auto	Mo	0.980	C	0.020
9	4000.00 A	auto	Mo	1.000		

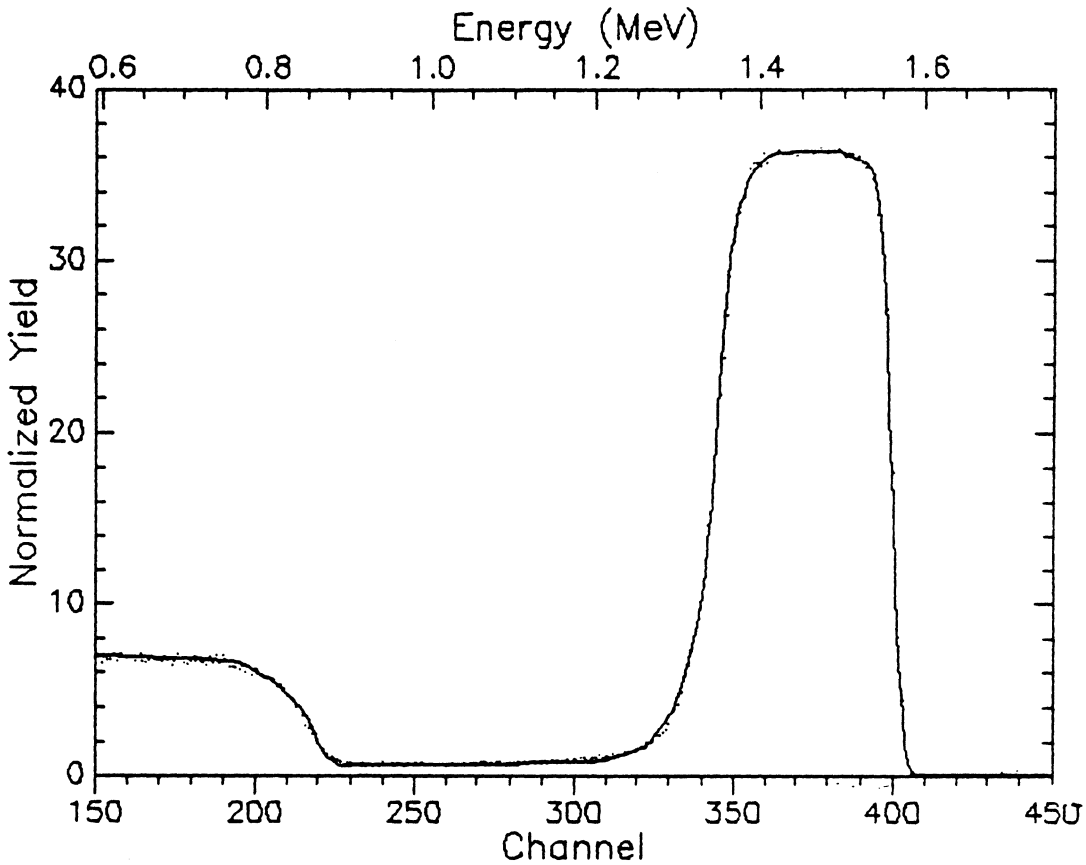


```
Current File: [RANGASW.SHENG]RUN103.RBS;1
Identifier:  Mo/Al as-deposited
                                        Date:  September 18, 1987
1.800 MeV     40.00 uCoulombs
Channel Energy Constants:      3.8790      10.5510
Correction Factor:    0.8900
Angles (Theta, Phi, Omega):    37.0000     45.0000    1.330
Livetime text:
Channel number of first data point:      0.0
Number of data points:  511
Detector FWHM:       20.0 keV        Beam: He+
RMS Beam current:    50.0 nA    Geometry: IBM
```

Figure 7. The metallic bilayer system Mo/Al as deposited.

Table 3. The metallic bilayer system Mo/Al as deposited.

#	Thickness	Sublayers	Composition . . .					
1	50.00 A	auto	Mo	0.900	C	0.100		
2	50.00 A	auto	Mo	0.950	C	0.050		
3	200.00 A	auto	Mo	1.000				
4	50.00 A	auto	Mo	0.940	Al	0.060		
5	50.00 A	auto	Mo	0.700	C	0.060	Al	0.240
6	50.00 A	auto	Mo	0.180	C	0.280	Al	0.540
7	50.00 A	auto	Mo	0.120	C	0.230	Al	0.650
8	50.00 A	auto	Mo	0.070	C	0.200	Al	0.730
9	100.00 A	auto	Mo	0.040	C	0.120	Al	0.800
10	100.00 A	auto	Mo	0.020	Al	0.980		
11	100.00 A	auto	Mo	0.015	Al	0.985		
12	400.00 A	auto	Mo	0.010	Al	0.990		
13	800.00 A	auto	Mo	0.007	Al	0.993		
14	6000.00 A	auto	Al	1.000				

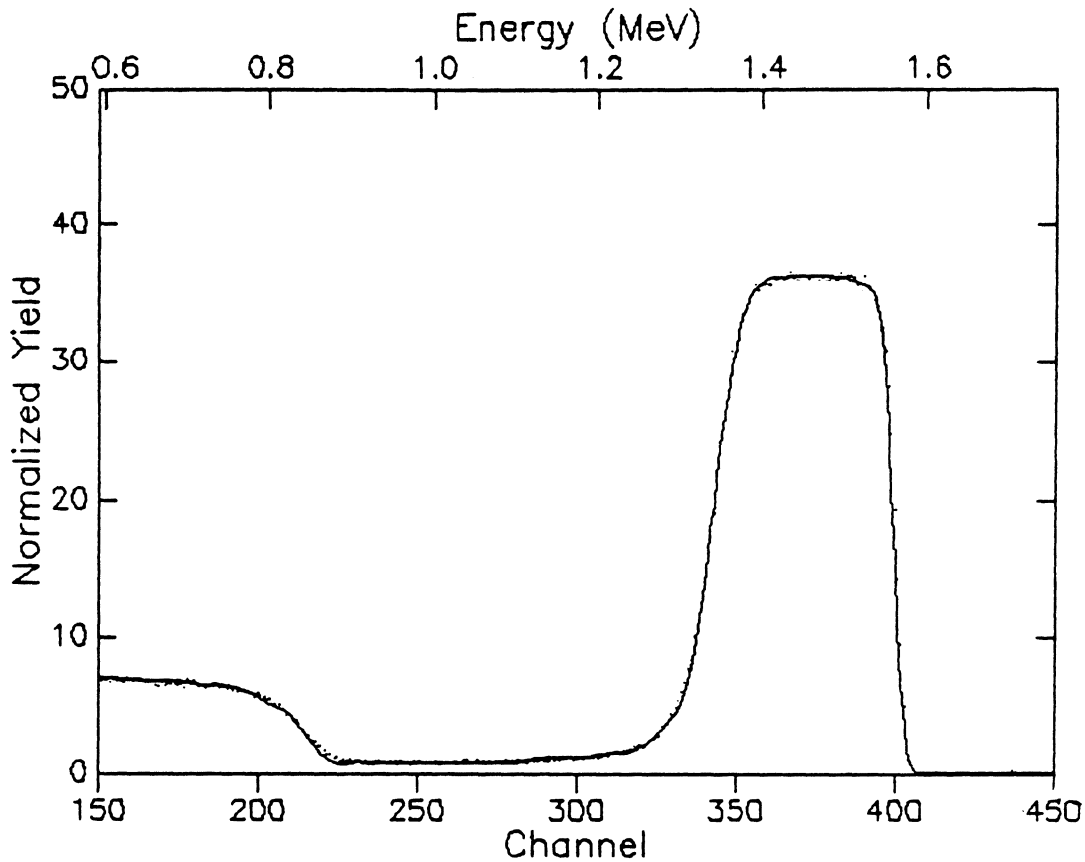

Current File: [RANGASW.SHENG]RUN107.RBS;1
Identifier: Mo/Al irradiated with dose 1e15
Date: September 18, 1987
1.800 MeV 40.00 uCoulombs
Channel Energy Constants: 3.8790 10.5510
Correction Factor: 0.7300
Angles (Theta, Phi, Omega): 37.0000 45.0000 1.330
Livetime text:
Channel number of first data point: 0.0
Number of data points: 513
Detector FWHM: 20.0 keV Beam: He+
RMS Beam current: 25.0 nA Geometry: IBM

Figure 8. Mo/Al sample irradiated with dose of 1×10^{15} /cm^2

Table 4. Mo/Al sample irradiated with dose of 1×10^{15} /cm^2

#	Thickness	Sublayers	Composition . . .					
1	50.00 A	auto	Mo	0.800	C	0.140		
2	50.00 A	auto	Mo	0.900	C	0.040		
3	50.00 A	auto	Mo	0.960	C	0.010		
4	160.00 A	auto	Mo	1.000				
5	50.00 A	auto	Mo	0.920	Al	0.080		
6	50.00 A	auto	Mo	0.700	C	0.300	Al	0.300
7	50.00 A	auto	Mo	0.350	C	0.400	Al	0.650
8	50.00 A	auto	Mo	0.150	C	0.400	Al	0.850
9	100.00 A	auto	Mo	0.070	C	0.300	Al	0.920
10	100.00 A	auto	Mo	0.035	C	0.100	Al	0.950
11	200.00 A	auto	Mo	0.020	C	0.050	Al	0.980
12	300.00 A	auto	Mo	0.015	Al	0.985		
13	830.00 A	auto	Mo	0.010	Al	0.990		
14	3000.00 A	auto	Al	1.000				

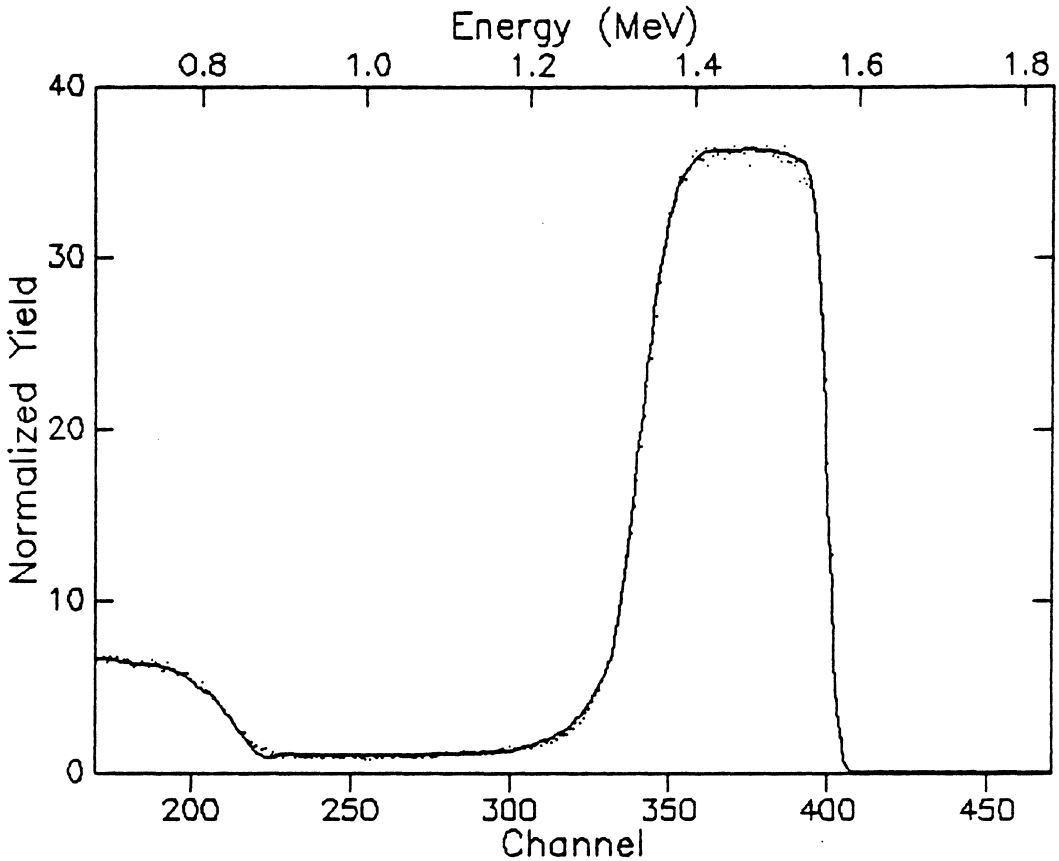


```
Current File: [RANGASW.SHENG]RUN110.RBS;1
Identifier: Mo/Al irradiated with dose 3e15
Date:  Sept.19, 1987
1.800 MeV    40.00 uCoulombs
Channel Energy Constants:    3.8790    10.5510
Correction Factor:   0.8200
Angles (Theta, Phi, Omega):   37.0000    45.0000   1.330
Livetime text:
Channel number of first data point:   -2.0
Number of data points:  513
Detector FWHM:     20.0 keV      Beam: He+
RMS Beam current:  25.0 nA   Geometry: IBM
```

Figure 9. Mo/Al sample irradiated with dose of 3×10^{15} /cm^2

Table 5. Mo/Al sample irradiated with dose of 3×10^{15} /cm^2

#	Thickness	Sublayers	Composition . . .					
1	50.00 A	auto	Mo	0.800	C	0.100		
2	50.00 A	auto	Mo	0.900	C	0.040		
3	50.00 A	auto	Mo	0.960	C	0.010		
4	160.00 A	auto	Mo	1.000				
5	50.00 A	auto	Mo	0.920	Al	0.080		
6	50.00 A	auto	Mo	0.820	C	0.120	Al	0.300
7	50.00 A	auto	Mo	0.480	C	0.200	Al	0.650
8	50.00 A	auto	Mo	0.250	C	0.350	Al	0.850
9	100.00 A	auto	Mo	0.100	C	0.300	Al	0.920
10	100.00 A	auto	Mo	0.050	C	0.100	Al	0.950
11	100.00 A	auto	Mo	0.032	C	0.040	Al	0.980
12	100.00 A	auto	Mo	0.025	C	0.050	Al	0.980
13	100.00 A	auto	Mo	0.017	C	0.019	Al	0.983
14	100.00 A	auto	Mo	0.016	C	0.020	Al	0.984
15	300.00 A	auto	Mo	0.014	Al	0.986		
16	630.00 A	auto	Mo	0.013	Al	0.987		
17	3000.00 A	auto	Al	1.000				

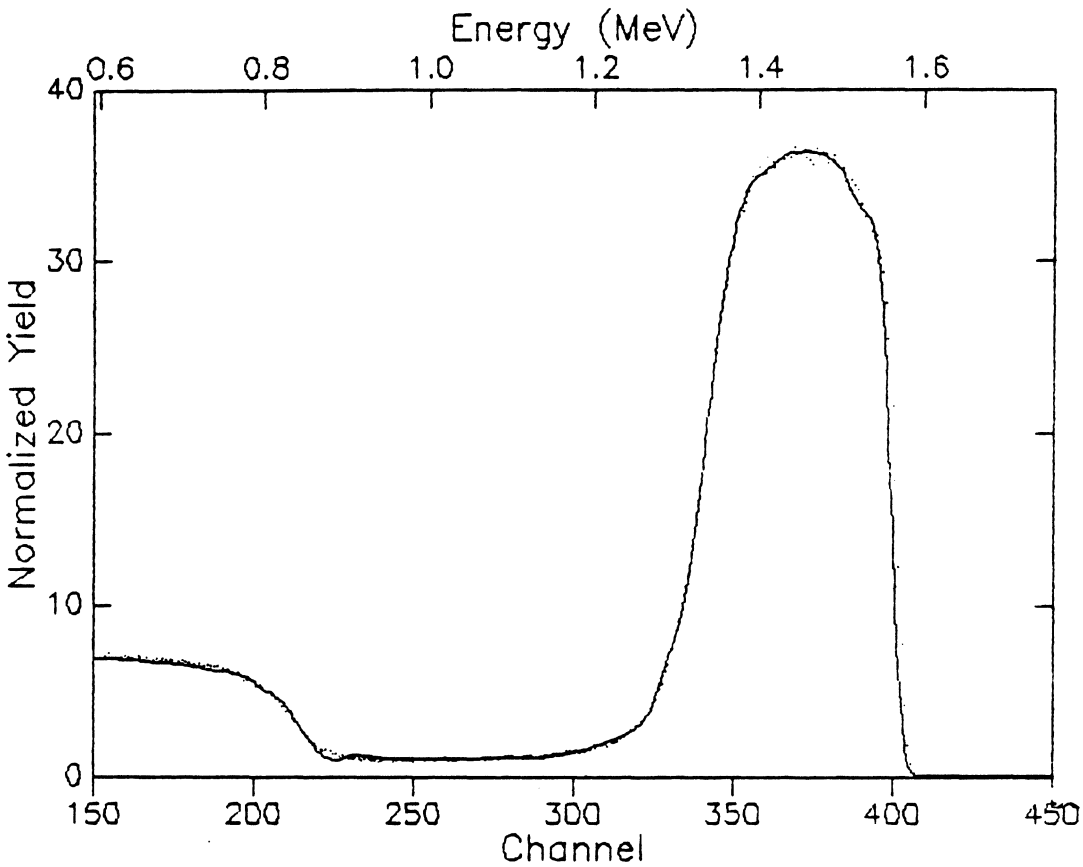


```
Current File: [RANGASW.SHENG]RUN113.RBS;1
Identifier:  Mo/Al irradiated with dose of 7e15
Date:  September 22, 1987
1.800 MeV     60.00 uCoulombs
Channel Energy Constants:     3.8790     10.5510
Correction Factor:   0.8900
Angles (Theta, Phi, Omega):    37.0000     45.0000    1.330
Livetime text:
Channel number of first data point:     0.0
Number of data points:  513
Detector FWHM:      20.0 keV       Beam: He+
RMS Beam current:   50.0 nA    Geometry: IBM
```

Figure 10. Mo/Al sample irradiated with dose of 7×10^{15} /cm^2

Table 6. Mo/Al sample irradiated with dose of 7×10^{15} /cm^2

#	Thickness	Sublayers	Composition . . .					
1	50.00 A	auto	Mo	0.800	C	0.350		
2	50.00 A	auto	Mo	0.900	C	0.300		
3	50.00 A	auto	Mo	0.960	C	0.050		
4	110.00 A	auto	Mo	1.000				
5	50.00 A	auto	Mo	0.950	Al	0.050		
6	50.00 A	auto	Mo	0.880	Al	0.120		
7	50.00 A	auto	Mo	0.700	C	0.120	Al	0.300
8	50.00 A	auto	Mo	0.480	C	0.200	Al	0.650
9	50.00 A	auto	Mo	0.250	C	0.230	Al	0.850
10	100.00 A	auto	Mo	0.130	C	0.160	Al	0.920
11	100.00 A	auto	Mo	0.050	C	0.100	Al	0.950
12	100.00 A	auto	Mo	0.035	C	0.070	Al	0.980
13	100.00 A	auto	Mo	0.028	C	0.040	Al	0.980
14	100.00 A	auto	Mo	0.020	C	0.019	Al	0.983
15	100.00 A	auto	Mo	0.016	C	0.020	Al	0.984
16	300.00 A	auto	Mo	0.014	Al	0.986		
17	630.00 A	auto	Mo	0.013	Al	0.987		
18	3000.00 A	auto	Al	1.000				

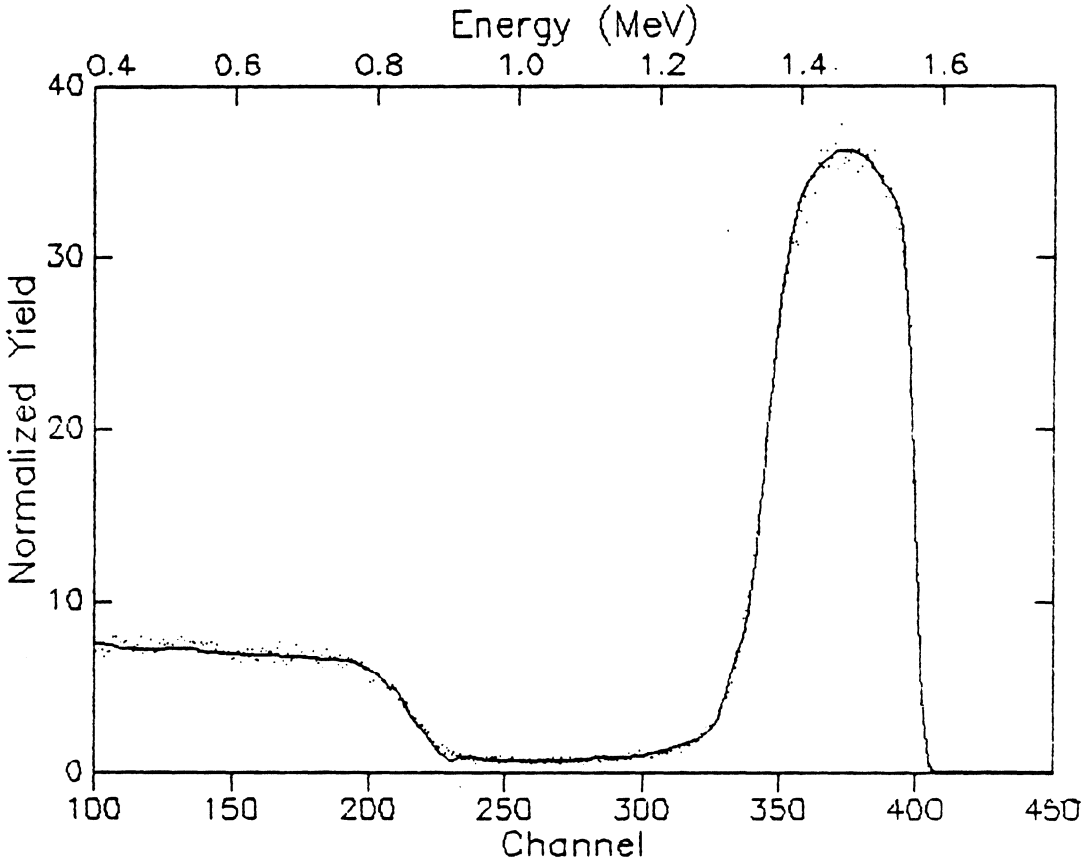

Current File: [RANGASW.SHENG]RUN118.RBS;1
Identifier: Mo/Al irradiated with dose of 11e15
Date: September 19, 1987
1.800 MeV 40.00 uCoulombs
Channel Energy Constants: 3.8790 10.5510
Correction Factor: 2.8600
Angles (Theta, Phi, Omega): 37.0000 45.0000 1.330
Livetime text:
Channel number of first data point: -2.0
Number of data points: 513
Detector FWHM: 20.0 keV Beam: He+
RMS Beam current: 15.0 nA Geometry: IBM

Figure 11. Mo/Al sample irradiated with dose of 7×10^{15} /cm^2

Table 7. Mo/Al sample irradiated with dose of 7×10^{15} /cm^2

#	Thickness	Sublayers	Composition . . .					
1	50.00 A	auto	Mo	0.800	C	0.300		
2	50.00 A	auto	Mo	0.900	C	0.230		
3	50.00 A	auto	Mo	0.960	C	0.050		
4	60.00 A	auto	Mo	1.000				
5	70.00 A	auto	Mo	0.950	Al	0.050		
6	50.00 A	auto	Mo	0.910	C	0.160	Al	0.090
7	50.00 A	auto	Mo	0.700	C	0.200	Al	0.300
8	50.00 A	auto	Mo	0.480	C	0.200	Al	0.650
9	50.00 A	auto	Mo	0.250	C	0.280	Al	0.850
10	100.00 A	auto	Mo	0.115	C	0.230	Al	0.885
11	100.00 A	auto	Mo	0.050	C	0.180	Al	0.950
12	100.00 A	auto	Mo	0.027	C	0.100	Al	0.973
13	120.00 A	auto	Mo	0.022	Al	0.978		
14	100.00 A	auto	Mo	0.018	Al	0.982		
15	100.00 A	auto	Mo	0.014	Al	0.986		
16	300.00 A	auto	Mo	0.012	Al	0.988		
17	630.00 A	auto	Mo	0.010	Al	0.990		
18	3000.00 A	auto	Al	1.000				

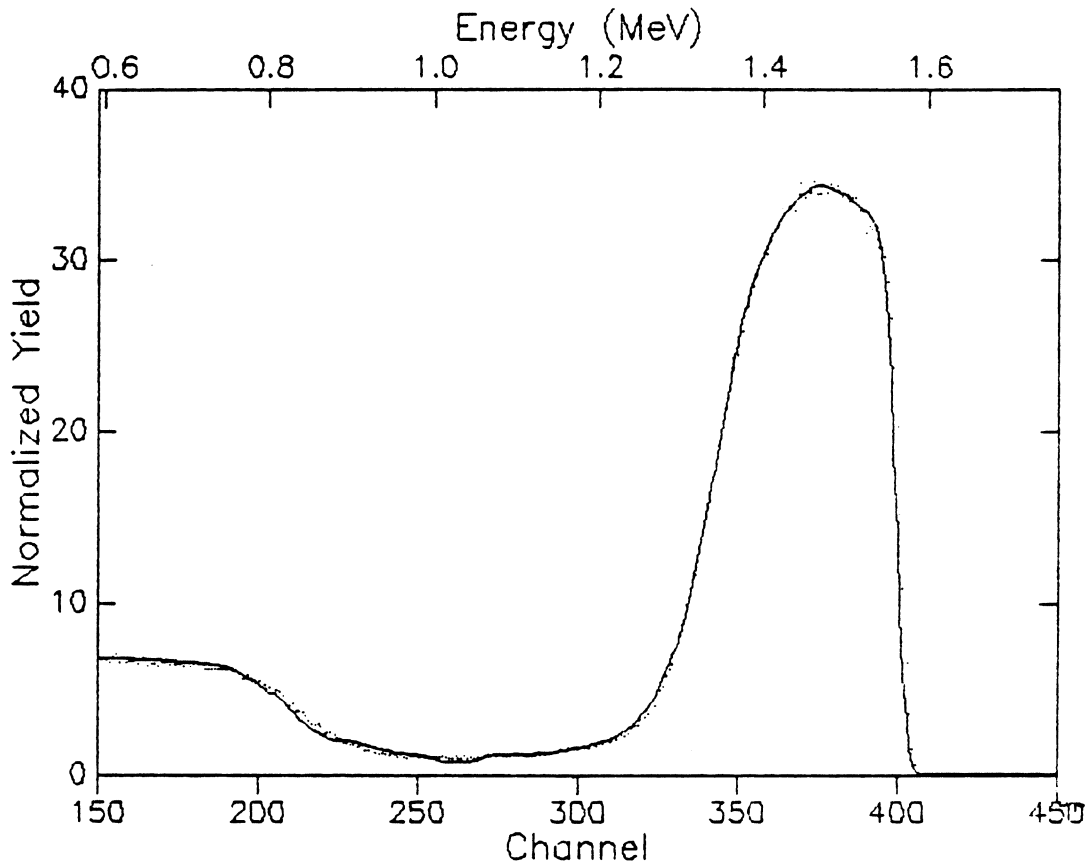

Current File: [RANGASW.SHENG]RUN120.RBS;1
Identifier: Mo/Al irradiated with dose 17e15
Date: September 18, 1987
1.800 MeV 40.00 uCoulombs
Channel Energy Constants: 3.8790 10.5510
Correction Factor: 0.8500
Angles (Theta, Phi, Omega): 37.0000 45.0000 1.330
Livetime text:
Channel number of first data point: 0.0
Number of data points: 513
Detector FWHM: 20.0 keV Beam: He+
RMS Beam current: 40.0 nA Geometry: IBM

Figure 12. Mo/Al sample irradiated with dose of 17×10^{15} /cm^2

Table 8. Mo/Al sample irradiated with dose of 17×10^{15} /cm^2

#	Thickness	Sublayers	Composition . . .					
1	50.00 A	auto	Mo	0.650	C	0.350		
2	50.00 A	auto	Mo	0.750	C	0.290		
3	50.00 A	auto	Mo	0.880	C	0.200		
4	50.00 A	auto	Mo	0.970	C	0.150	Al	0.030
5	50.00 A	auto	Mo	0.870	Al	0.130		
6	50.00 A	auto	Mo	0.800	Al	0.200		
7	50.00 A	auto	Mo	0.700	Al	0.300		
8	50.00 A	auto	Mo	0.580	Al	0.420		
9	50.00 A	auto	Mo	0.430	C	0.150	Al	0.570
10	50.00 A	auto	Mo	0.310	C	0.240	Al	0.690
11	50.00 A	auto	Mo	0.210	C	0.250	Al	0.790
12	100.00 A	auto	Mo	0.120	C	0.200	Al	0.880
13	100.00 A	auto	Mo	0.060	C	0.100	Al	0.940
14	100.00 A	auto	Mo	0.036	Al	0.964		
15	100.00 A	auto	Mo	0.028	Al	0.972		
16	100.00 A	auto	Mo	0.023	Al	0.977		
17	100.00 A	auto	Mo	0.018	Al	0.982		
18	300.00 A	auto	Mo	0.016	Al	0.984		
19	630.00 A	auto	Mo	0.010	Al	0.990		
20	3000.00 A	auto	Al	1.000				

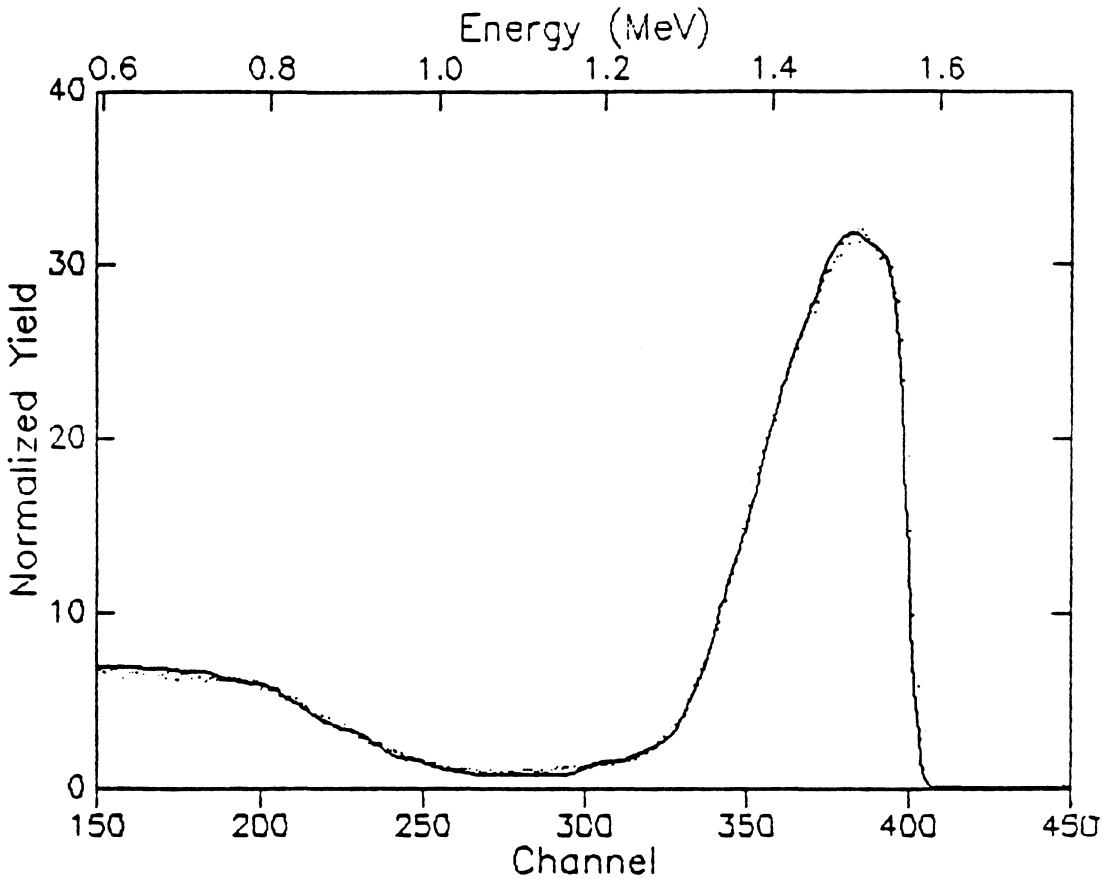

Current File: [RANGASW.SHENG]RUN127.RBS;1
Identifier: Mo/Al irradiated with dose of 30.2e15
Date: September 23, 1987
1.800 MeV 40.00 uCoulombs
Channel Energy Constants: 3.8790 10.5510
Correction Factor: 0.9100
Angles (Theta, Phi, Omega): 37.0000 45.0000 1.330
Livetime text:
Channel number of first data point: 0.0
Number of data points: 513
Detector FWHM: 20.0 keV Beam: He+
RMS Beam current: 80.0 nA Geometry: IBM

Figure 13. Mo/Al sample irradiated with dose of 30.2×10^{15} /cm^2

Table 9. Mo/Al sample irradiated with dose of 30.2×10^{15} /cm^2

#	Thickness	Sublayers	Composition . . .					
1	50.00 A	auto	Mo	0.600	C	0.400		
2	50.00 A	auto	Mo	0.640	C	0.360		
3	50.00 A	auto	Mo	0.750	C	0.250	Al	0.050
4	50.00 A	auto	Mo	0.740	C	0.200	Al	0.130
5	50.00 A	auto	Mo	0.650	C	0.100	Al	0.350
6	50.00 A	auto	Mo	0.540	C	0.050	Al	0.460
7	50.00 A	auto	Mo	0.440	Al	0.560		
8	50.00 A	auto	Mo	0.350	Al	0.650		
9	50.00 A	auto	Mo	0.290	C	0.200	Al	0.710
10	50.00 A	auto	Mo	0.240	C	0.200	Al	0.760
11	50.00 A	auto	Mo	0.190	C	0.200	Al	0.810
12	50.00 A	auto	Mo	0.120	C	0.200	Al	0.880
13	50.00 A	auto	Mo	0.090	C	0.200	Al	0.910
14	50.00 A	auto	Mo	0.060	C	0.100	Al	0.940
15	100.00 A	auto	Mo	0.040	C	0.100	Al	0.960
16	100.00 A	auto	Mo	0.030	C	0.100	Al	0.970
17	200.00 A	auto	Mo	0.020	Al	0.980		
18	800.00 A	auto	Mo	0.010	Al	0.990		
19	3000.00 A	auto	Al	1.000				

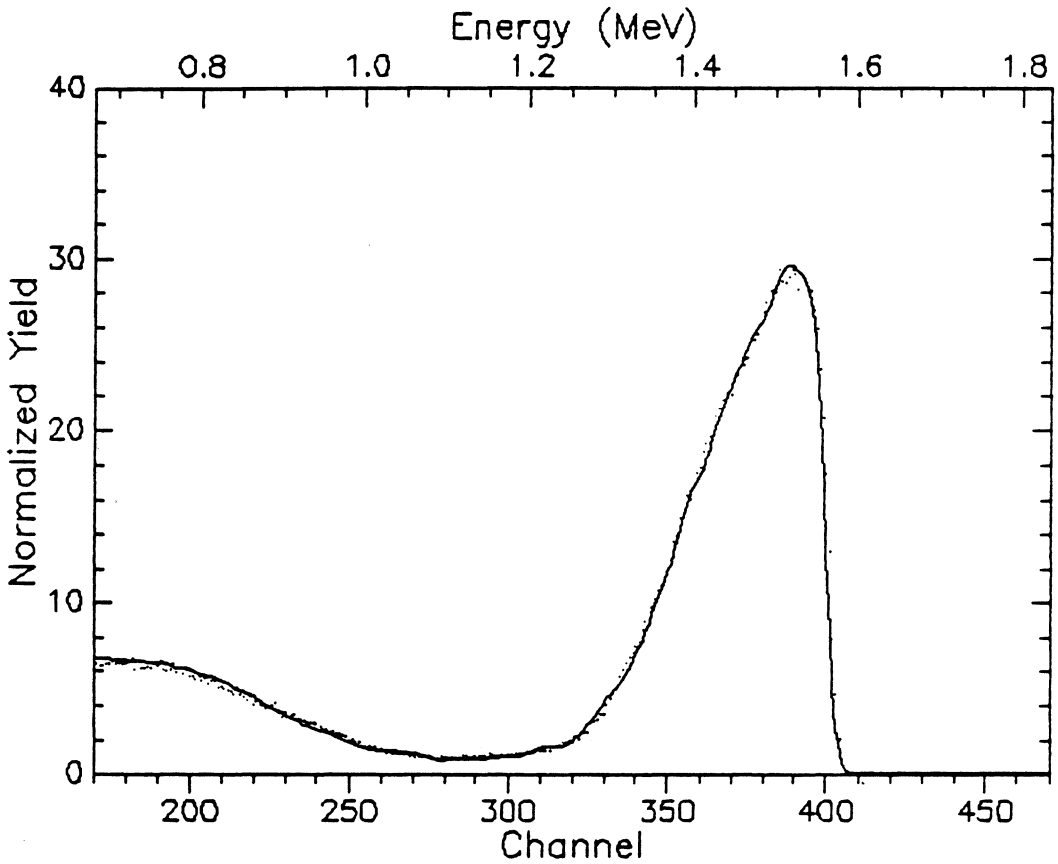

Current File: [RANGASW.SHENG]RUN129.RBS;1
Identifier: Mo/Al irradiated with dose of 40.2e15
Date: September 23, 1987
1.800 MeV 40.00 uCoulombs
Channel Energy Constants: 3.8790 10.5510
Correction Factor: 0.8400
Angles (Theta, Phi, Omega): 37.0000 45.0000 1.330
Livetime text:
Channel number of first data point: -1.0
Number of data points: 513
Detector FWHM: 20.0 keV Beam: He+
RMS Beam current: 50.0 nA Geometry: IBM

Figure 14. Mo/Al sample irradiated with dose of 40.2×10^{15} /cm^2

Table 10. Mo/Al sample irradiated with dose of 40.2×10^{15} /cm^2

#	Thickness	Sublayers	Composition . . .					
1	50.00 A	auto	Mo	0.610	Al	0.390	C	1.400
2	50.00 A	auto	Mo	0.600	Al	0.400	C	0.800
3	50.00 A	auto	Mo	0.610	Al	0.390	C	0.500
4	50.00 A	auto	Mo	0.560	Al	0.440	C	0.250
			Xe	0.170				
5	50.00 A	auto	Mo	0.490	Al	0.510	C	0.170
			Xe	0.130				
6	50.00 A	auto	Mo	0.420	Al	0.580	C	0.130
			Xe	0.100				
7	50.00 A	auto	Mo	0.360	Al	0.640	C	0.080
			Xe	0.095				
8	50.00 A	auto	Mo	0.320	Al	0.680	C	0.070
			Xe	0.092				
9	50.00 A	auto	Mo	0.270	Al	0.730	C	0.070
			Xe	0.070				
10	50.00 A	auto	Mo	0.220	Al	0.780	C	0.050
			Xe	0.056				
11	50.00 A	auto	Mo	0.190	Al	0.810	C	0.040
			Xe	0.053				
12	50.00 A	auto	Mo	0.140	Al	0.860	C	0.030
			Xe	0.025				
13	50.00 A	auto	Mo	0.110	Al	0.890	C	0.030
			Xe	0.040				
14	50.00 A	auto	Mo	0.090	Al	0.910	C	0.028
			Xe	0.017				
15	100.00 A	auto	Mo	0.070	Al	0.930	C	0.024
			Xe	0.009				
16	100.00 A	auto	Mo	0.040	Al	0.960	C	0.020
			Xe	0.006				
17	200.00 A	auto	Mo	0.022	Al	0.978		
18	200.00 A	auto	Mo	0.013	Al	0.987		
19	260.00 A	auto	Mo	0.011	Al	0.989		
20	3000.00 A	auto	Al	1.000				

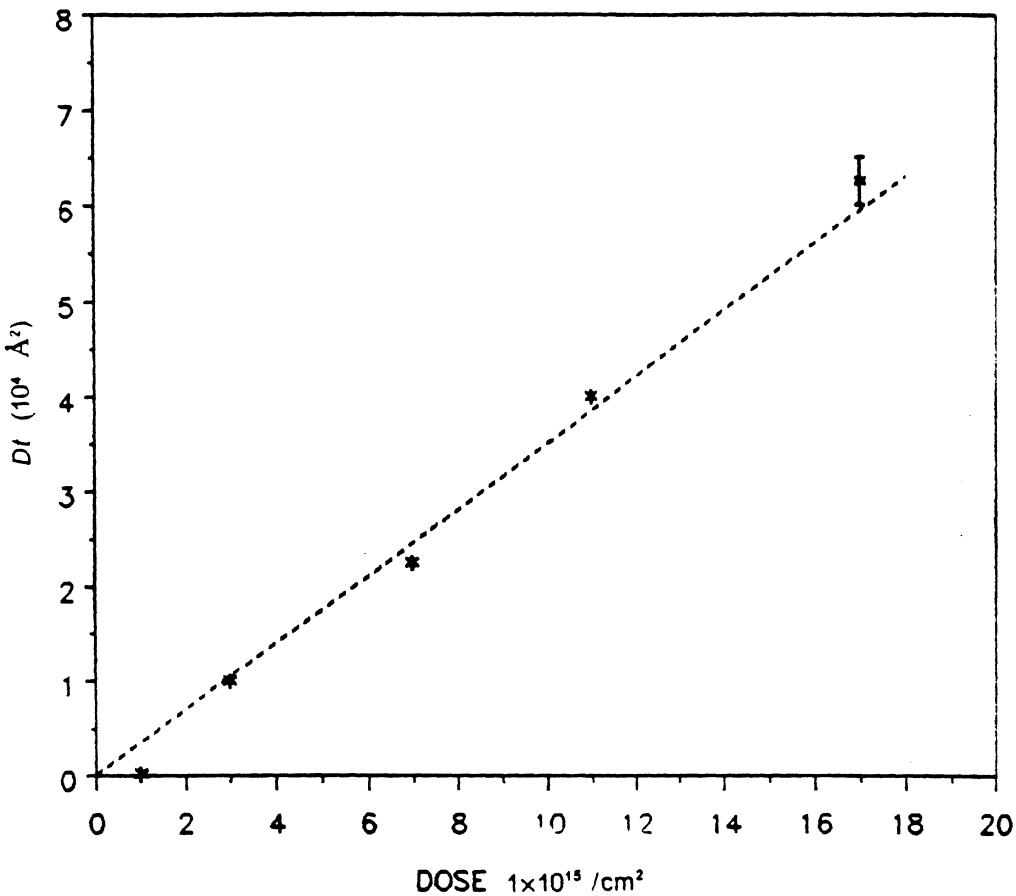

Figure 15. The effective diffusion length for metallic bilayer of Mo/Al irradiated with different doses.

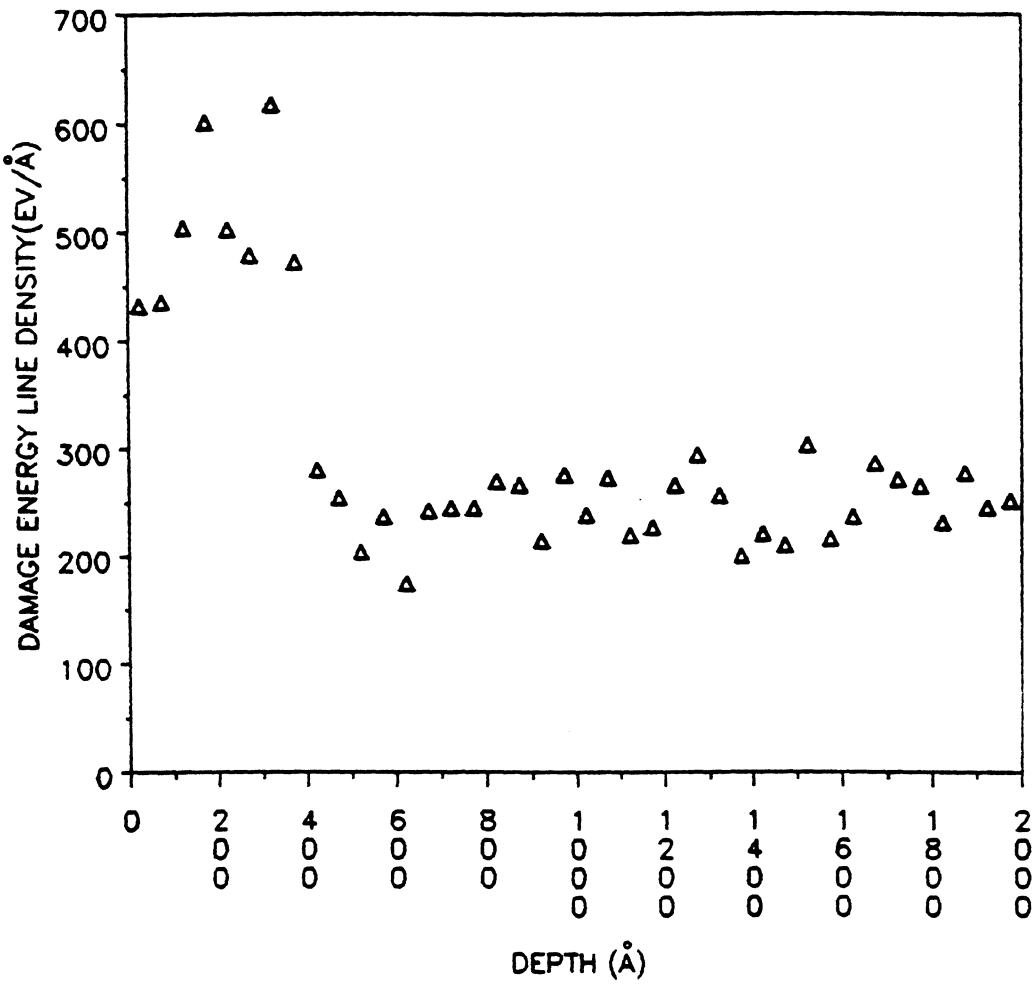

Figure 16. The damage energy line density distribution with depth for metallic bilayer sample Mo/Al irradiated with 1.8 MeV Xe ions.

4.0 Thermal Spike Induced Mixing and Related Nonlinear Effects

4.1 Introduction

Thermal spike, energy spike, or the high density cascade region are terms which usually mean the same thing, although they are used to describe and interpret various mixing mechanisms and physical models. Here it will be referred to as "spike ". As early as 1956 Seitz and Koehler [31] suggested that the local "hot spot" concept existed in a lattice, which is in fact similar to the cascade picture. Recently after an extensive study of ballistic mixing, researchers realized that it is the spike that plays the dominating role in most of the heavy bombardment mixing cases. In these cases, the ballistic mixing always underestimates the ion beam mixing results, even with the more sophisticated ballistic mixing theories [4]. Good quantitative or semi-quantitative analysis of spike induced atomic transport has been behind the experimental work. The Cal Tech group, Cheng et al [16], recognized that the thermochemical effect was significant in metallic bilayer samples which had been subjected to heavy bombardment. From similar research work [15,17], it was found that Darken's

chemically driven diffusion analysis was still suitable for thermally activated atomic transport in the spike region. However, their adopted Vineyard's spike model is very rough and a more detailed analysis is necessary.

The ion beam induced atomic transport is composed of three different mechanisms, namely:

(i) ballistic mixing: in the first stage of ion beam bombardment, atoms in regular positions are displaced from their original position via recoil collisions and cascade collisions;

(ii) Thermal spike induced short-range diffusion: immediately after the ballistic mixing there is a partial annealing phase located in the spike region which lasts up to 10^{-10} s. During this phase the contribution by the short-ranged radiation-induced diffusion is significant;

(iii) Radiation enhanced diffusion: after the thermal spike process ends the assembly of agitated atoms is still in a non-equilibrium state. Consequently, the point defects will move towards sinks where they annihilate their anti-particles. This process continues until an equilibrium state is achieved.

In order to gain a better physical understanding of spike and spike related phenomena, many attempts have been made to characterize spike-induced atomic transport. The ideas which will be developed in the following are:

(i) the improved formulation of Vineyard cylindrical spike model,

(ii) the suggested spherical spike,

(iii) spike shapes with different extents of collisional cascade as compared with the experimental data,

(iv) point defect creation in the spike region,

(v) thermochemically activated diffusion in the spike region, and

(vi) point defect partial annealing in the spike volume during the spike periods.

4.2 The Modified Vineyard's Cylindrical Model

Thermal spike is normally described as a limited volume with the majority of atoms temporarily in motion as a result of collisional cascades, i.e., thermal spikes only occur in a limited region in which high density cascades or overlapping of subcascades exist. It has been estimated that the characteristic kinetic energy in the spike region is of the order of a few electronvolts per particle [38], and its equivalent temperature is of several thousands Kelvins. As a phenomenological analyses of the thermal spike diffusion effect, a suggested model is based on the Vineyard's spike idea [32]. In addition, the point defect partial annealing is considered to occur in the thermal spike region. Here some of results introduced in section 2.5, chapter 2 will be used directly in order to save space.

The number of point defects created by collisional displacement is an important factor. This quantity can be estimated using the Kinchin-Pease formula [30], equation (2-15).

The short-term partial annealing will cause annihilation of some of the migrating point defects. Let τ_v , τ_i denote the vacancy and interstitial point defects lifetimes respectively in the irradiated materials. Here the lifetime of the point defect refers to the time period which begins as the thermal spike begins and ends once the point defects have either annihilate with their anti-particle or to be trapped by their sinks (e.g., grain boundary, dislocation et al). τ_v , τ_i depend on both the density of sinks and the density of anti-particles around them. We assume the latter plays an important role, especially for the high density cascade cases. As a rough estimate, τ_v or τ_i may be taken to be about 10^{-11} s or 10^{-12} s [26]. Then the number of jumps per unit volume per unit time can be expressed by

$$\Gamma = \alpha_v e^{-\frac{t}{\tau_v}}(A_v + \frac{0.42F_D}{E_d})e^{-\frac{Q_v}{T(r,t)}} + \alpha_i e^{-\frac{t}{\tau_i}}(A_i + \frac{0.42F_D}{E_d})e^{-\frac{Q_i}{T(r,t)}} \qquad (4-1)$$

where

α_v is vacancy-jumping frequency per unit cross section in the spike region.

α_i is interstitial-jumping frequency per unit cross section in the spike region.

A_v is the number of vacancies per unit path length in the cascade area which initially existed in the as-deposited material,

A_i is the number of interstitials per unit path length in the cascade area which initially existed inside the as-deposited material,

Q_v and Q_i are migration energies for the vacancies and interstitials respectively. This quantities can be scaled by the cohesive energy of the materials as assumed by Johnson et al [2].

It is convenient to consider the cases when there is only one dominating mechanism, either a vacancy mechanism or an interstitial mechanism. This procedure clearly retains the generality of the diffusion mechanism, so Γ_c can be expressed as:

$$\Gamma_c = \frac{0.42\alpha F_D}{E_d} e^{-\frac{t}{\tau}} e^{-\frac{Q}{T(r,t)}} \qquad (4-2)$$

where

α is jump frequency per unit cross section in the spike regions.

τ is the lifetime of the point defect,

Q is the migration energy of the point defect.

In equation (4-2) we neglect the contribution coming from the point defects which initially existed at low temperatures in the as-deposited sample, since their number is much smaller than the number of point defects produced in the collisional cascade process. Next the total number of jumps induced in one spike per unit length of the cylindrical spike cab be can be calculated and is denoted by η_c

$$\eta_c = \int_0^\infty 2\pi r dr \int_0^\infty \Gamma_c dt \qquad (4-3)$$

$$\eta_c = \frac{0.42\alpha F_D^3}{4\pi\kappa Q^2 c E_d}\left[\frac{1}{H_c^2}\ln(1+H_c) - \frac{1}{H_c} + \frac{1}{H_c+1}\right] \qquad (4-4)$$

where

$$H_c = \frac{F_D}{4\pi Q\kappa\tau} \qquad (4-5)$$

The parameter H_c is dimensionless. It characterizes the short-term annealing process which is due to the point defects migration and annihilation with their anti-particles in the thermal spike periods. H_c will be increased when the lifetime τ is decreased, which means the point defect annihilating process are more significant. When the damage energy parameter increases, the H_c-parameter also increases, which not only means that thermal spike effect increases as a result of increased cascade density, but also the spike triggered point defect annealing effect is increased. As a rough estimate take $F_D = 100eV/\text{Å}$ for the typical thermal spike dominated ion beam mixing and $\kappa = 0.1$ to 10 $Wcm^{-1}K^{-1}$ for metal elements, the estimated parameter $H_c = 10^{-1}$ to 10^{-3} . After performing the Taylor expansion up to the fourth order of F_D term, the equation (4-4) becomes

$$\eta_c \simeq \frac{0.42\alpha F_D^3}{4\pi\kappa Q^2 c E_d}\left(1 - \frac{4}{3}H_c\right) \qquad (4-6)$$

The total number of jumps in the materials after being irradiated with dose Φ is then $\eta_c\Phi/\rho$, ρ is the atomic density of the target material (cm^{-3}). The typical jumping distance r_c can be related to ρ, $< r_c^2 > = q_1\rho^{-2/3}$. Moreover the migration energy Q may be scaled by the cohesive energy of the matrix, i.e., $Q = -q_2\Delta H_{coh}$. According to the definitions of displacement energy and cohesive energy of materials, it can be assumed that the displacement energy of the target E_d can also be scaled by ΔH_{coh} , $E_d = -q_3\Delta H_{coh}$. Then the diffusion

characteristic parameter Dt/Φ is proportional to $\eta_c < r_c^2 > /\rho$, or the mixing parameter can be characterized by the following equation

$$\frac{(D_T^c + D_A^c)t}{\Phi} = \frac{B_1}{\rho^{5/3}}\left(\frac{F_D}{\Delta H_{coh}}\right)^3\left(1 - \frac{4}{3}H_c\right) \qquad (4-7)$$

where

D_T^c is the effective diffusion coefficient corresponding to thermal spike induced atomic migration,

D_A^c is the effective diffusion coefficient corresponding to short-term partial annealing inside the cascade volumes,

B_1 is a constant related to κ, c, and q_1, q_2, q_3.

If $H_c << 1$, then

$$L_T^c \equiv \frac{D_T^c t}{\Phi} = \frac{B_1}{\rho^{5/3}}\left(-\frac{F_D}{\Delta H_{coh}}\right)^3 \qquad (4-8)$$

Here L_T^c is defined as the thermal spike-induced mixing parameter. For the more general case, the ballistic mixing should also be included and is characterized by L_b

$$L_b \equiv \frac{D_b t}{\Phi} = \frac{0.42 < r_c^2 >}{6\rho E_d} F_D \qquad (4-9)$$

where D_b is the effective diffusion coefficient corresponding to ballistic mixing.

or

$$L_b = \frac{0.42}{6} B_2 \rho^{5/3}\left(-\frac{F_D}{\Delta H_{coh}}\right) \qquad (4-10)$$

where B_2 is a constant and is related to q_1, q_3.

The total mixing parameter can be written as

$$L = L_b + L_T^c + L_A^c \qquad (4-11)$$

where

$$L_A^c = -\frac{B_3}{\rho^{5/3}}\left(-\frac{F_D}{\Delta H_{coh}}\right)^4 \qquad (4-12)$$

or

$$L_A^c = -\frac{4}{3}H_c L_T^c \qquad (4-13)$$

where

B_3 is a constant, and is related to c, κ, τ, q_1, q_2, and q_3.

L_A^c is the mixing parameter related to the short-term partial annealing of the point defects during thermal spike period.

This effect suppresses the thermal spike-induced diffusion process and thus attributes a negative value to the thermal spike inducing ion mixing. But this contribution to the whole ion mixing is normally much smaller than the spike-induced diffusion efficiency, then it may be neglected in usual cases. In the following data comparison we no longer consider the mixing parameter L_A^c induced by the short-term annealing, this is suitable to experimental data we used. Only in the extreme cases when H_c is nearly equal to one or even greater than one, the short-term annealing induced mixing is significant, i.e., the thermal spike induced diffusion is suppressed greatly by the point defect partial annealing.

4.3 The Spherical Spike

From the cascade shapes and sizes simulation in FCC metals [33], and the analysis of cascade and related spikes by a fractal-geometry approach [14], it is more reasonable to

assume that the spike is shaped like the superposition of spherical spike component and cylindrical spike component. The spherical model may be a suitable estimate in the normal ion beam mixed metallic systems.

To derive the spherical spike formula the similar procedure was followed as above. Suppose a single isolated cascade dimension is λ, and λ is a constant for a similar series of metallic targets. From Kinchin-Pease formula we obtain the number of displaced atoms per unit path length n at the spike site

$$n = \frac{0.42E_D}{\lambda E_d} \qquad (4-15)$$

The initial conditions for the heat conduction equation (2-6) are

$$T(R, 0_-) = 0 \qquad (4-16)$$

$$T(R, 0_+) = \frac{E_D}{c}\delta^3(R) \qquad (4-17)$$

where

$\delta^3(R)$ is the three dimension δ-function in spherical coordinate,

R is the radius of spherical coordinate.

The environment temperature is taken to be zero as assumed in cylindrical model above. The boundary condition is

$$T(R, t)|_{R\to\infty} = 0 \qquad (4-18)$$

The solution to the heat conduction equation is

$$T(R,t)=\frac{E_D c^{3/2}}{8(\pi\kappa t)^{3/2}}e^{-\frac{cR^2}{4\kappa t}} \qquad (4-19)$$

The number of jumps per unit volume per unit time Γ_c in equation (4-2) can be used for the spherical spike model by substituting F_D with E_D/λ. Then the total number of jumps induced by one spike per unit path length of the spike for spherical model is

$$\eta_s=\int_0^\infty 2\pi R dR\int_0^\infty \frac{0.42\alpha E_D}{E_d\lambda}e^{-\frac{t}{\tau}}e^{-\frac{Q}{T(R,t)}}dt \qquad (4-20)$$

Here we consider the diffusional jumps in the circle area with radius R parallel to the surface plane, and the direction of the atomic jump in this area is perpendicular to this area. Then

$$\eta_s=\frac{0.42\alpha\lambda^{4/3}}{4\pi c^{1/3}\kappa E_d}[\frac{1}{2}\Gamma(\frac{4}{3})F_D^{2+\frac{1}{3}}Q^{-4/3}-\frac{\lambda^{2/3}c}{12\pi\tau\kappa Q^2}F_D^3] \qquad (4-21)$$

where $\Gamma(x)$ is the gamma-function. The thermal spike mixing parameter for spherical-shaped spike is

$$L_T^s\equiv\frac{D_T^s t}{\Phi}=\frac{G_1}{\rho^{5/3}}(-\frac{F_D}{\Delta H_{coh}})^{2+\frac{1}{3}} \qquad (4-22)$$

where G_1 is a constant and is related to c, κ, λ, q_1, q_2, and q_3.

The point defect partial annealing induced mixing parameter L_A^i is

$$L_A^S = -\frac{G_2}{\rho^{5/3}}\left(-\frac{F_D}{\Delta H_{coh}}\right)^3 \qquad (4-23)$$

where G_2 is also a constant similar to G_1

or

$$L_A^S = -H_S L_T^S \qquad (4-24)$$

where

$$H_S = \frac{\lambda^{2/3} c^{1/3}}{6\pi\tau\kappa\Gamma(\frac{4}{3})}\left(\frac{F_D}{Q}\right)^{2/3} \qquad (4-25)$$

As an estimate of H_s, take $\lambda = 100\text{Å}$, c = 1 $Jcm^{-3}K^{-1}$ to 10 w $cm^{-3}K^{-1}$, $\tau = 10^{-11}$ s , $F_D = 500eV/\text{Å}$, then $H_s = 10^{-1}$ to 10^{-3} . Clearly, the point defect partial annealing gives little influence to the ion induced mixing process, and is neglected in the normal cases. This is the same as the cylindrical model.

In reality the spike shape is neither ideally cylindrical or ideally spherical, they may be in between. In another word, the spike shape should be the superposition of the spherical component and the cylindrical component.

From the cylindrical and spherical spike model developed above, we proposed that the parameter $(-F_D/\Delta H_{coh})$ is suitable to characterize the spike process and related phenomena. In fact, $(-F_D/\Delta H_{coh})$ is proportional to the number of point defects per unit path length in the damaged region, referred to as the point defect line density parameter ($\chi = -F_D/\Delta H_{coh}$). For the ballistic mixing the mixing parameter L_b is linear-dependent on χ; for the thermal spike induced diffusional process the mixing parameter $D_T t/\Phi$ is proportional to $\chi^{2+\mu}$ (μ will be determined in the following). Obviously, the thermal spike gives the nonlinear effect on the total mixing parameter. This nonlinear effect comes from the coupling of large number of point defects in the cascade region and the thermal spike field (described by the

temperature distribution). In another sense, the induced diffusional term can be regarded as the interaction between the ballistic mixing and thermal spike.

4.4 Chemical Effects

For the irregular solid solution, chemical interaction plays an important role. Johnson et al [2] expressed the chemical biased random walk process by multiplying the Darken term, which means the random walking is also driven by chemical forces in the non-ideal solutions. Thus the number of jumps per unit volume per unit time in equation (4-2) for cylindrical shaped spike becomes

$$\tilde{\Gamma}_c = \frac{0.42\alpha F_D}{E_d} e^{-\frac{t}{\tau}} e^{-Q/T(r,t)} [1 - 2\frac{\Delta H_m}{T(r,t)}] \qquad (4-26)$$

where ΔH_m is the heat of mixing of the target materials.

If we do not consider the point defect partial annealing effect the derived formula for cylindrical model characterized by the number of jumps per unit length for one spike is

$$\tilde{\eta}_c = \frac{0.42\alpha F_D^3}{4\pi\kappa Q^2 c E_d}(1 - 4\frac{\Delta H_m}{Q}) \qquad (4-27)$$

Similarly as before, the mixing parameter can be expressed as

$$\tilde{L}_T^c \equiv \frac{\tilde{D}_T^c t}{\Phi} = \frac{B_1}{\rho^{5/3}}(-\frac{F_D}{\Delta H_{coh}})^3(1 + J_c\frac{\Delta H_m}{\Delta H_{coh}}) \qquad (4-28)$$

where J_c is a new constant and related to q_2 only.

For spherical spike model, the chemical driven diffusional process can be similarly described by $\tilde{\eta}_s$

$$\tilde{\eta}_s = \frac{0.42\Gamma(\frac{4}{3})\lambda^{4/3}}{8\pi c^{1/3}\kappa E_d Q^{4/3}}(1 - \frac{8\Delta H_m}{3Q}) \qquad (4-29)$$

Then the mixing parameter for the spherical spike diffusional process aided by chemical biased diffusion is

$$\tilde{L}_T^s \equiv \frac{\tilde{D}_T^s t}{\Phi} = \frac{G_1}{\rho^{5/3}}(-\frac{F_D}{\Delta H_{coh}})^{2+\frac{1}{3}}(1 + J_s\frac{\Delta H_m}{\Delta H_{coh}}) \qquad (4-30)$$

where J_s is a constant similar to J_c, and related to q_2 only.

Compare equation (4-28) and (4-30) these mixing parameters have similar driving force-induced diffusion contribution for the cylindrical spike model and spherical spike model. The two constants, $J_c = \frac{4}{q_2}$ for the cylindrical spike, $J_s = \frac{8}{3q_2}$ for the spherical spike, does not make much difference to the phenomenological analysis. The formulae derived here are similar to the original development suggested by Johnson et al [2]. The only difference between the modified cylindrical spike model, or the spherical spike model, and the original Vineyard's cylindrical model lies in the power dependence of $(-\frac{F_D}{\Delta H_{coh}})^{2+\mu}$; $\mu = 0$ is the Vineyard's original cylindrical model, $\mu = 1$ is the modified cylindrical model, $\mu = 1/3$ is the spherical model suggested here.

4.5 The Density of Displaced Atoms

In the binary collision approximation the point defects created in the collisional cascade process can be expressed by the Kinchin-Pease model (equation (2-15)). But this formula is only valid in low density cascade region. In the case of extremely high density of cascades, the cascade region becomes liquid-like, and the molecular dynamics dominates the physical processes, such as the collective motions of neighboring atoms. Thus the Kinchin-Pease model will no longer sufficient to characterize the point defect density in the high density cascade region. A semi-empirical formulation was developed by Thompson and Walker[9] in studying thermal spikes in Silicon and Germanium. They suggested that the defects generated by high-bombardment be comprised of two components, point defects generated by collisonal cascades and thermal spike related defects component. A semi-empirical formulation was obtained for the number of defects created in cascade region, as described in Chapter 2, equation (2-16).

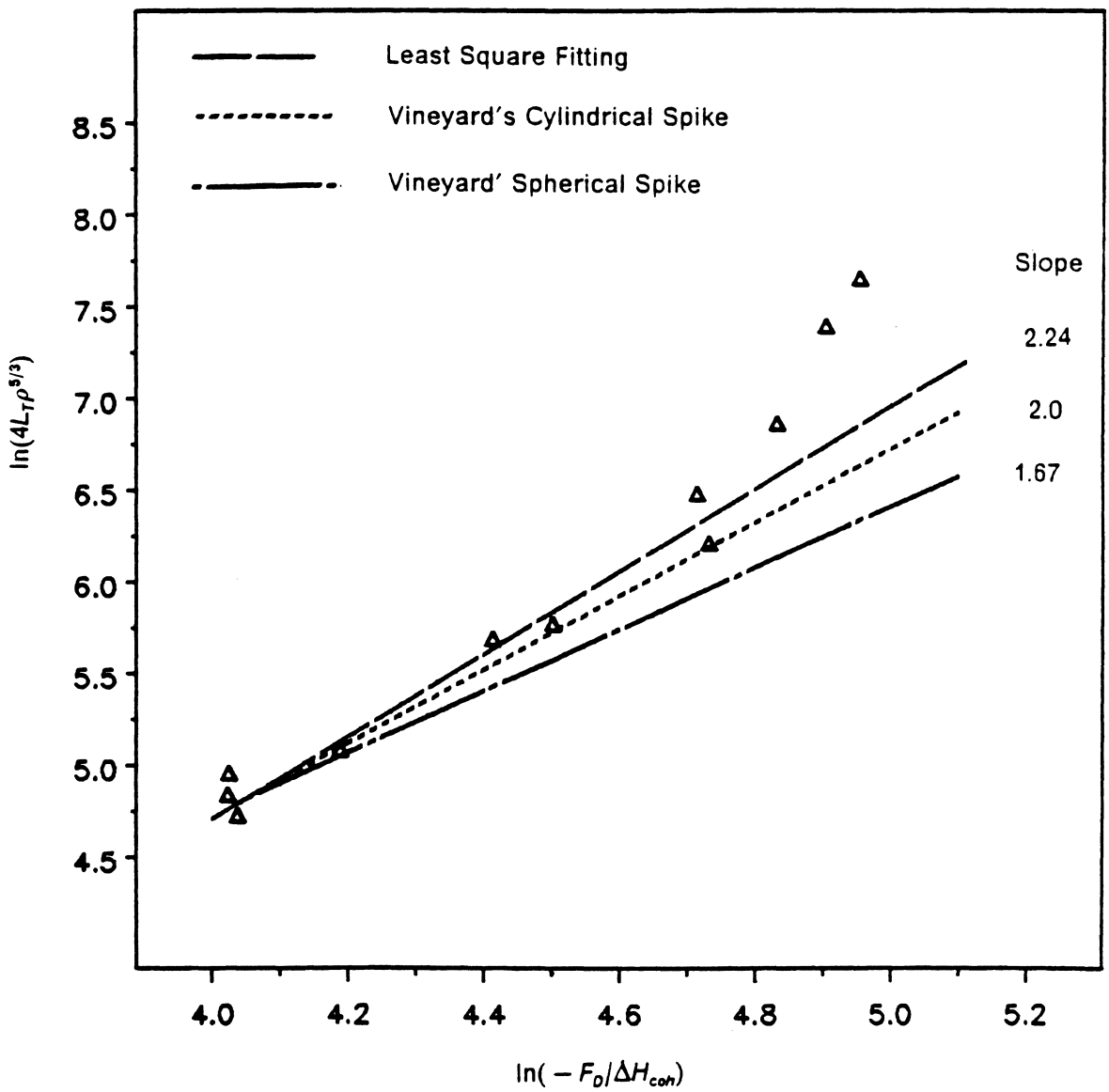

Figure 17. The log-plot to find out the power factor μ in metallic bilayer ion mixing. The plot is in the form of $\ln(4L_T\rho^{5/3})$ to $\ln(-F_D/\Delta H_{coh})$. The data are from ref. [15,16].

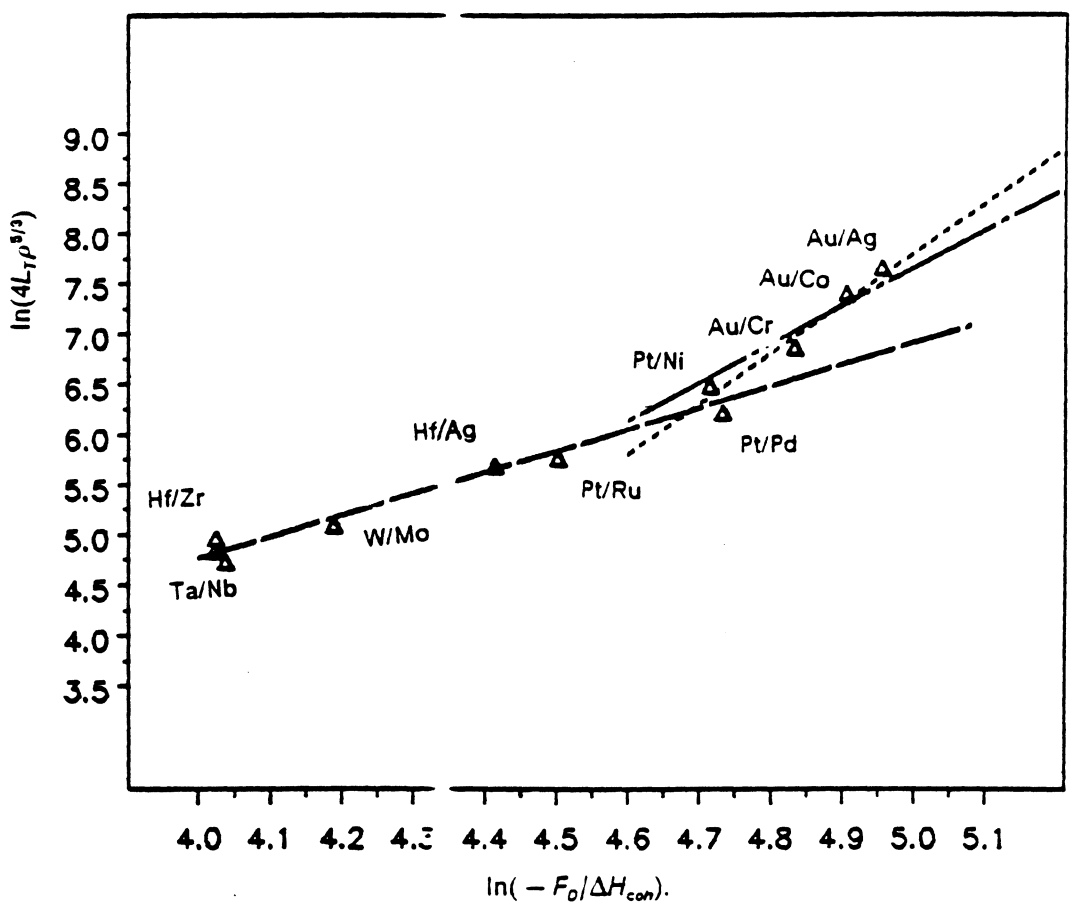

Figure 18. The log-plot to find out the power factor μ in metallic bilayer ion mixing. The plot is in the form of $\ln(4L_T\rho^{5/3})$ to $\ln(-F_D/\Delta H_{coh})$. The data are from ref. [15,16].

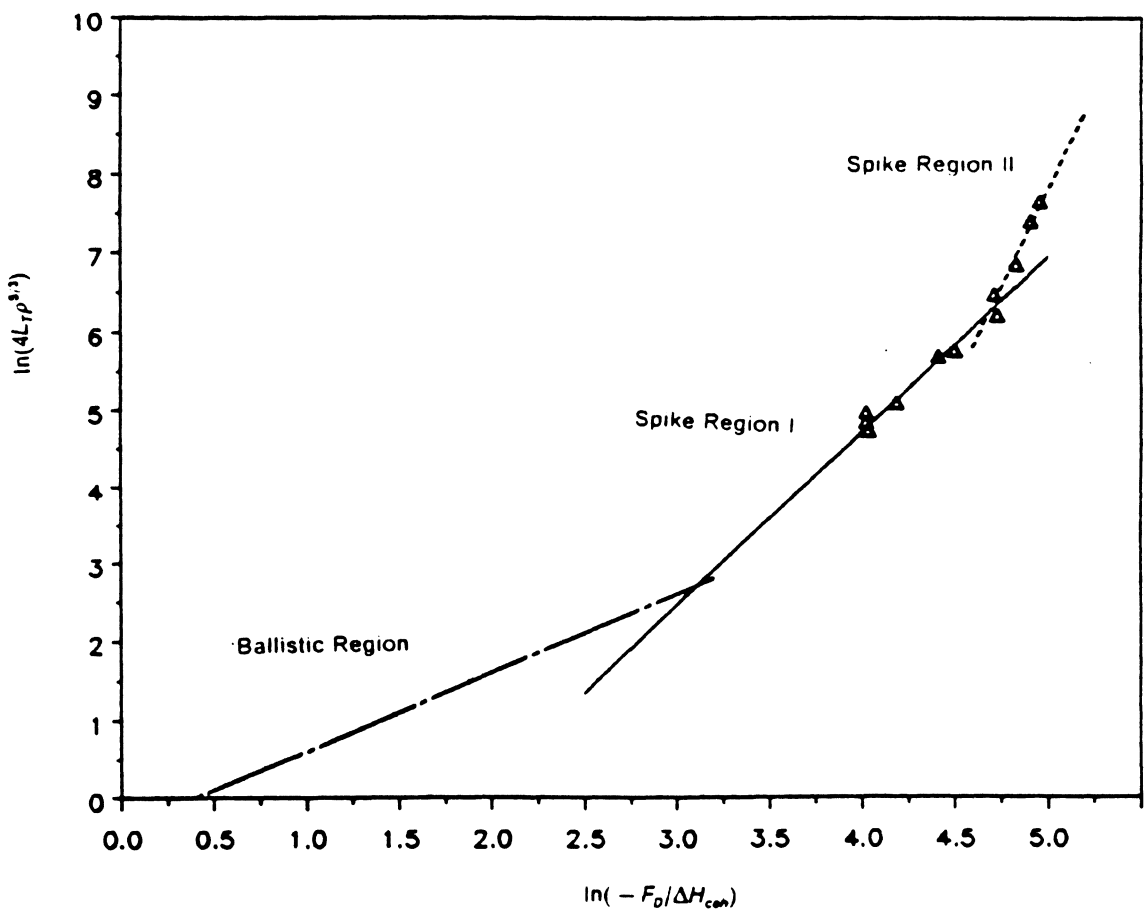

Figure 19. The log-plot to find out the different regions of ion mixing in metallic bilayer samples. The plot is in the form of $\ln(4L_T\rho^{5/3})$ to $\ln(-F_D/\Delta H_{coh})$. The data are from ref. [15,16].

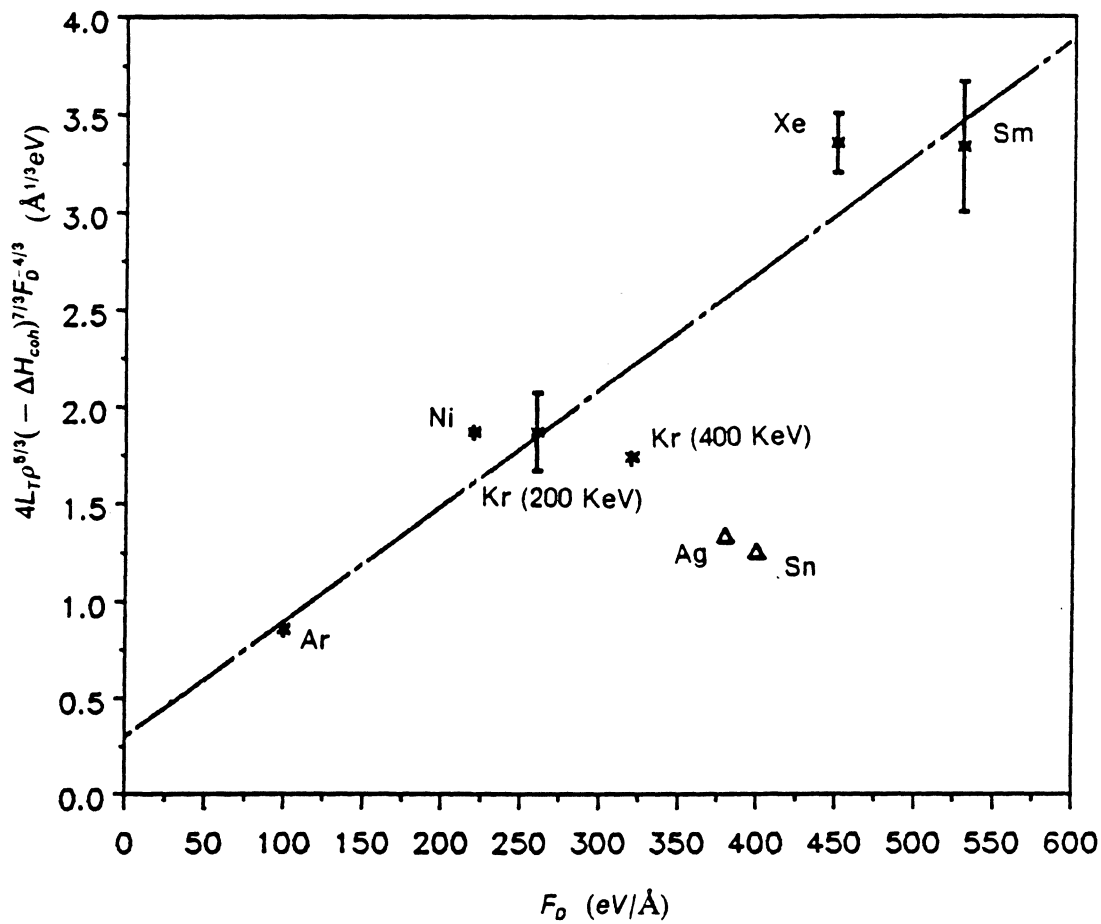

Figure 20. The spherical model was used in correlating data for metallic marker layer experiments. The plot is $4L_T\rho^{5/3}/F_D^{4/3}$ to F_D(eV/Å). The data are from ref. [6]. The data point Ne was ommited since the spike effect is not as dominant as the ballistic mixing in the case of Ne ion irradiation.

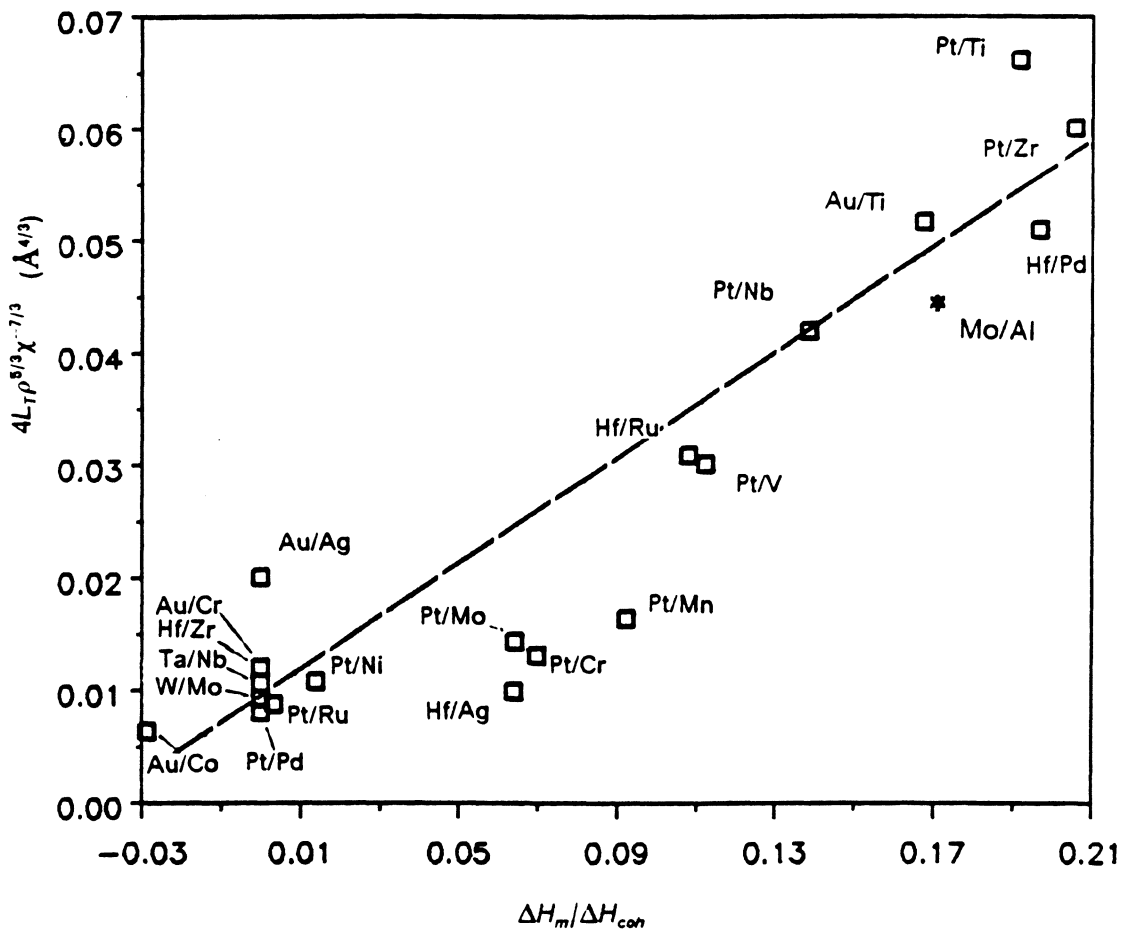

Figure 21. The plot of chemical related mixing effect during ion beam mixing for the metallic bilayer system. The spherical spike model was adopted in this plot. The horizontal axis is $\Delta H_m/\Delta H_{coh}$. The vertical axis is $4L_T\rho^{5/3}(-F_D/\Delta H_{coh})^{-2.3}$.

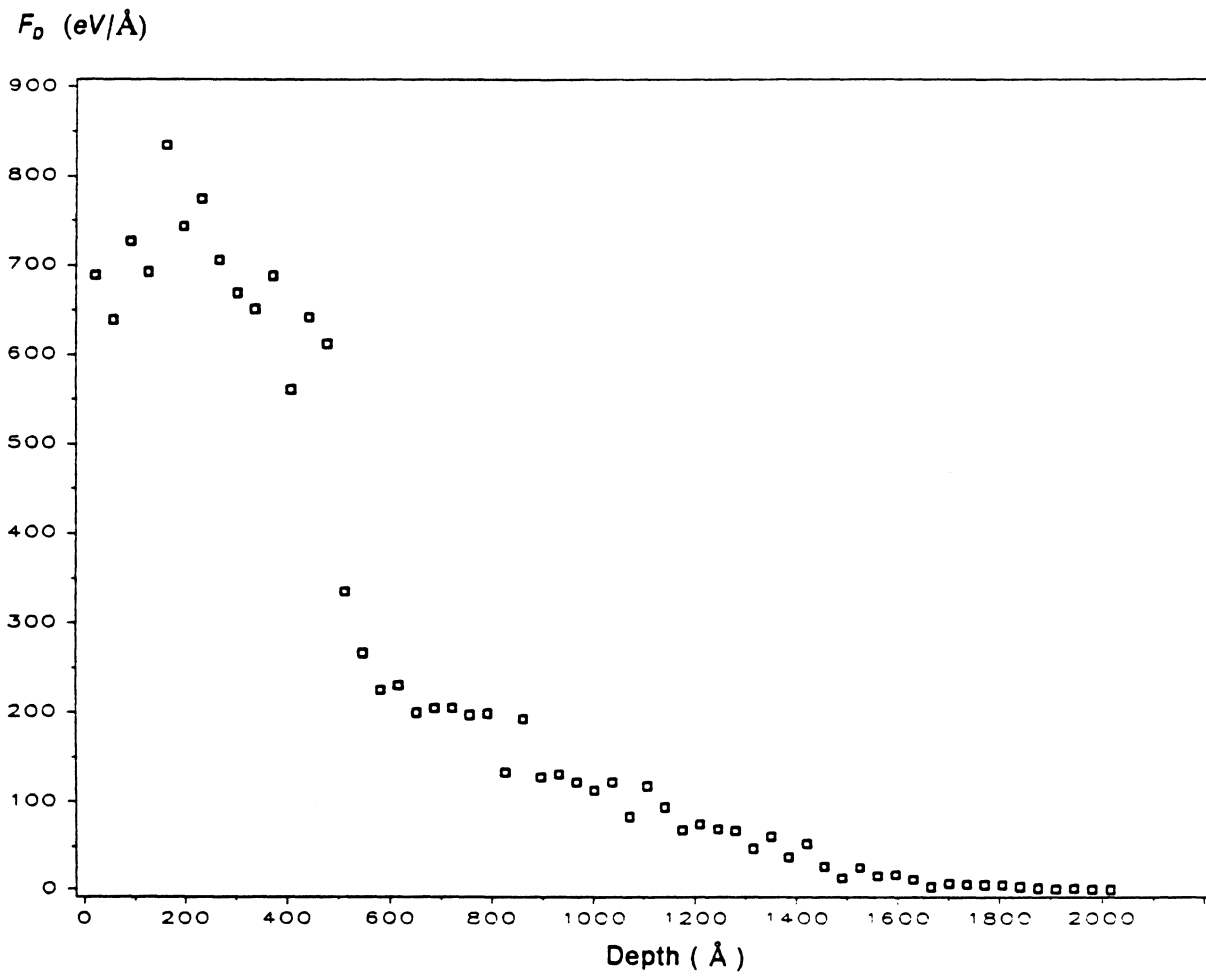

Figure 22. The damage energy line density distribution is plotted with depth after using the TRIM code program. This figure shows the typical plot to obtain F_D used in the spike model developed in the Chapter 4.

Table 11. Metallic bilayer system subjected to the heavy-bombardment of 600 KeV Xe ion [15,16].

This data was used for the Log-plot in figure 17, that is, $\ln(4L_T\rho^{5/3})$ to $\ln\chi$

system	$-\Delta H_m$ (kj/g.at)	$-\Delta H_{coh}$ (eV/atom)	F_D (eV/Å)	ρ (Å^{-3})	$4L_T$ (Å^4)	$\ln\chi$	$\ln(4L_T\rho^{5/3})$
Pt/Ni	7.	5.21	582.	0.0788	0.45	4.7159	6.4797
Hf/Ag	31.	5.02	415.	0.0519	0.41	4.4148	5.6906
Pt/Ru	2.	6.31	570.	0.0699	0.27	4.5035	5.7691
Au/Co	-11	3.99	539.	0.0743	0.45	4.9060	7.3950
Pt/Pd	0.	4.87	554.	0.0671	0.45	4.7341	6.2118
Hf/Zr	0.	6.34	355.	0.0440	0.26	4.0252	4.9599
W/Mo	0.	7.86	519.	0.0636	0.16	4.1901	5.0884
Ta/Nb	0.	7.84	445.	0.0556	0.14	4.0388	4.7309
Au/Ag	0.	3.38	480.	0.0588	2.37	4.9559	7.6531
Au/Cr	0.	3.96	498.	0.0712	0.78	4.8344	6.8607
Hf/Zr	0.	6.35	355.	0.0441	0.23	4.0237	4.8411

Table 12. Metallic marker layer Pd(200 Å)/Pt(5 Å)/Pd mixed with different incident ions at low temperatures[6].

Incident Ion	Q_T (Å^5/eV)	F_D (eV/Å)	$4L_T\rho^{5/3}(-\Delta H_{coh})^{7/3}F_D^{-4/3}$ (Å$^{1/3}$eV)
Ar (200 KeV)	0.9	100	0.857
Ni (200 KeV)	2.5	220	1.87
Kr (200 KeV)	2.7 ± 0.6	260	1.87 ± 0.2
Kr (400 KeV)	2.7	320	1.74
Ag (200 KeV)	2.2	380	1.34
Sn (200 KeV)	2.1	400	1.26
Xe (400 KeV)	5.8 ± 0.25	450	3.35 ± 0.15
Sm (400 KeV)	6.1 ± 0.6	530	3.33 ± 0.33

Here the atomic density for Pd is $\rho = 6.77 \times 10^{-2}$ Å^{-3}, the cohesive energy of Pd is $-\Delta H_{coh} = 3.89$ eV/atom, the ballistic mixing efficiency obtained by the computer code TRALL[27] is $Q_b = 7.0$ Å^5/eV, and then the spike-induced mixing efficiency was calculated by $Q_T = Q_0 - Q_b = \frac{L_T}{F_D}$.

Table 13. Metallic bilayer systems subjected to heavy-bombardment of 600 KeV Xe ion[15,16].

(Here $Y = 4L_T\rho^{5/3}\chi^{-7/3}$)

system	$-\Delta H_m$	$-\Delta H_{coh}$	F_D	ρ	$4L_T$	$\Delta H_m/\Delta H_{coh}$	Y
	(kj/g.at)	(eV/atom)	(eV/Å)	($Å^{-3}$)	($Å^4$)		($Å^{4/3}$)
Pt/Ti	122.	6.60	445.	0.0614	1.28	0.1917	0.0661
Pt/V	68.	6.27	491	0.0692	0.68	0.1125	0.0302
Pt/Mn	43.	4.82	531.	0.0740	0.73	0.0925	0.0164
Pt/Cr	36.	5.34	530.	0.0747	0.45	0.0699	0.0131
Pt/Ni	7.	5.21	582.	0.0788	0.45	0.0139	0.0108
Au/Ti	84.	5.20	414.	0.0578	1.63	0.1675	0.0517
Au/Co	-11.	3.99	539.	0.0743	0.45	-0.0286	0.0063
Pt/Zr	151.	7.61	480.	0.0546	1.21	0.2058	0.0600
Hf/Pd	122.	6.43	440.	0.0566	1.17	0.1968	0.0510
Pt/Nb	104.	7.78	515.	0.0609	0.79	0.1387	0.0420
Hf/Ru	77.	7.39	450.	0.0594	0.50	0.1081	0.0310
Pt/Mo	42.	6.77	540.	0.0652	0.37	0.0643	0.0143
Hf/Ag	31.	5.02	415.	0.0519	0.41	0.0641	0.0099
Pt/Ru	2.	6.31	570.	0.0699	0.27	0.0033	0.0087
Pt/Pd	0.	4.87	554.	0.0671	0.45	0.0000	0.0080
Hf/Zr	0.	6.34	355.	0.0440	0.26	0.0000	0.0119
W/Mo	0.	7.86	519.	0.0636	0.16	0.0000	0.0092
Ta/Nb	0.	7.84	445.	0.0556	0.14	0.0000	0.0092
Au/Ag	0.	3.38	480.	0.0588	2.37	0.0000	0.0200
Au/Cr	0.	3.96	498.	0.0712	0.78	0.0000	0.0120
Hf/Zr	0.	6.35	355.	0.0441	0.23	0.0000	0.0106

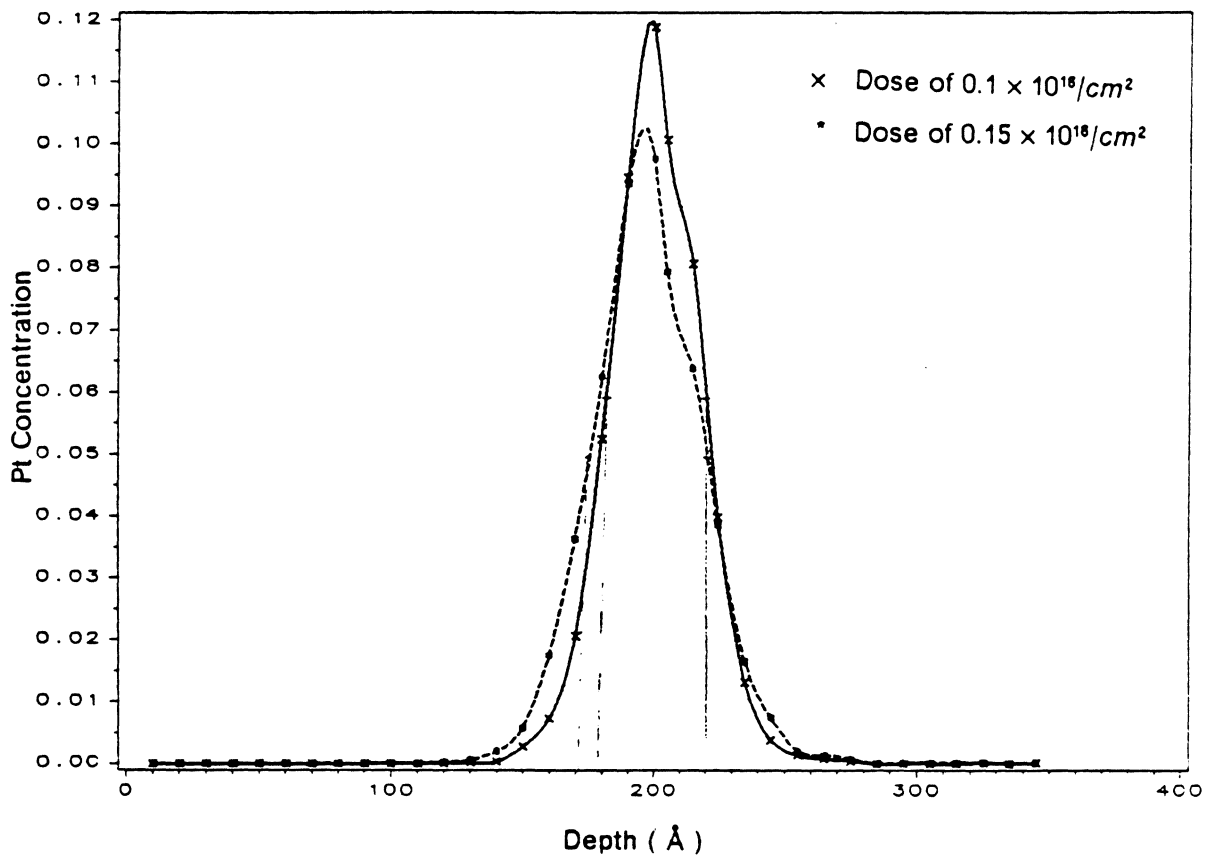

Figure 23. Marker layer Pt embeded in Pd matrices is mixed by 200 KeV Ni. This is at low temperatures and is predicted by the computer code TRALL. The experimental data is from the ref. [6]. The doses are $0.1 \times 10^{16}/cm^2$ and $0.15 \times 10^{16}/cm^2$.

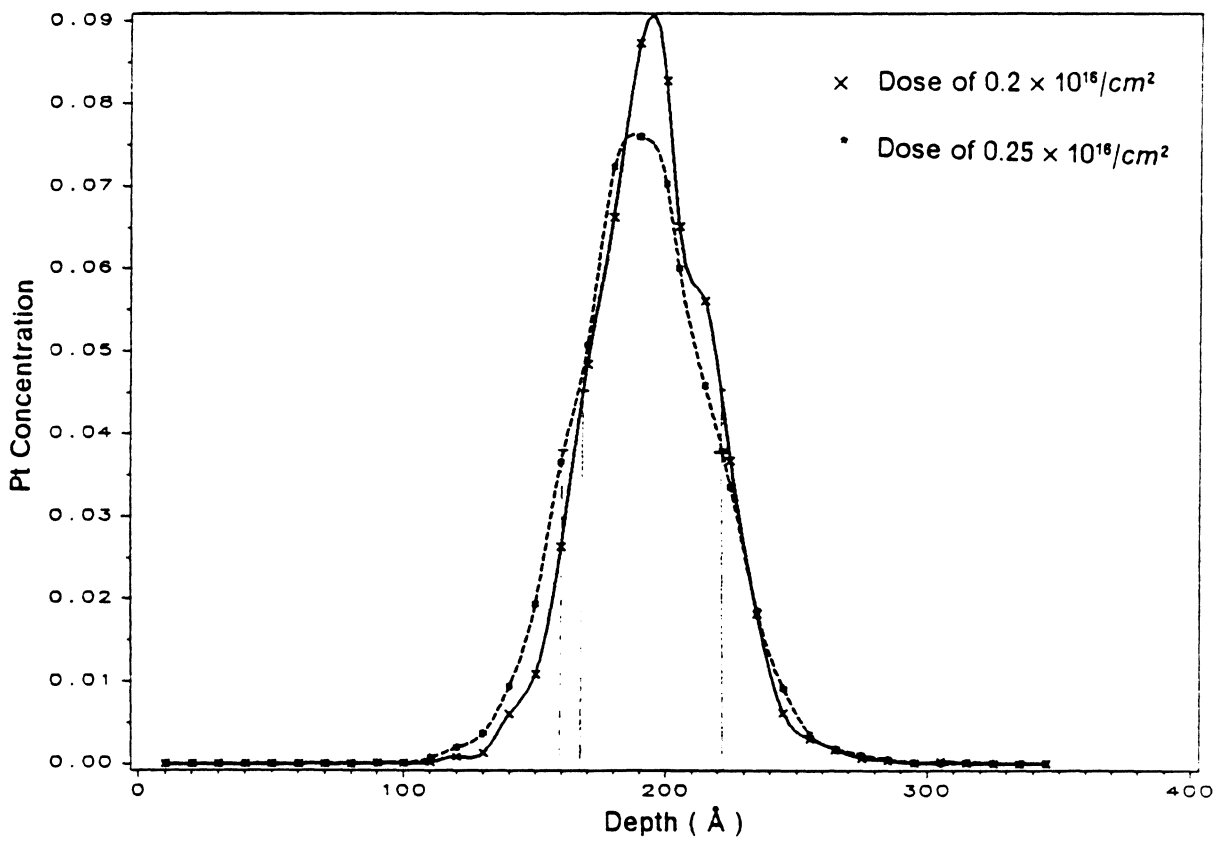

Figure 24. The profile of marker layer Pt embeded in Pd matrices after being mixed by 200 KeV Ni. This is at low temperatures and is predicted by the computer code TRALL. The experimental data is from the ref [6]. The doses are $0.2 \times 10^{16}/cm^2$ and $0.25 \times 10^{16}/cm^2$.

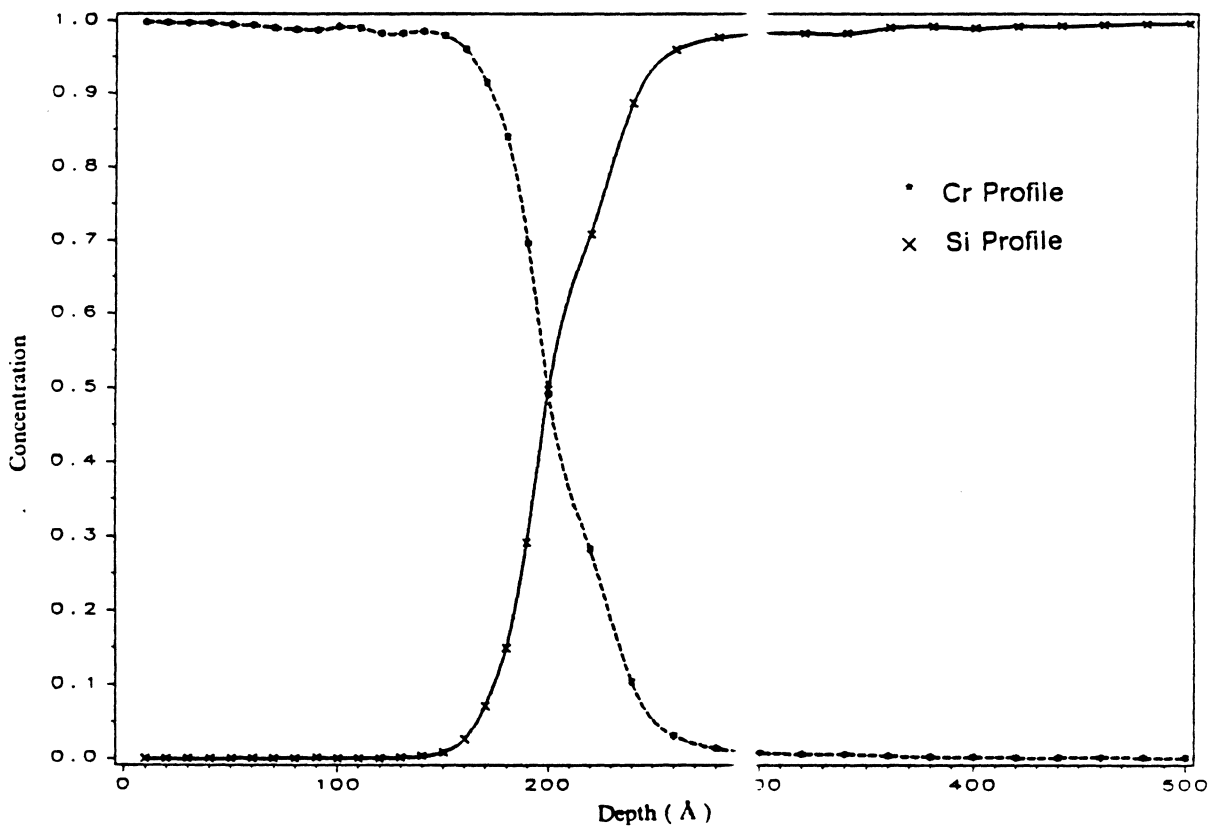

Figure 25. The composition profile of bilayer syster Cr/Si implanted with 45 KeV Cr. This is the plot predicted by the cor puter code TRALL for dose of $0.3 \times 10^{16}/cm^2$. The experiment is from re [37].

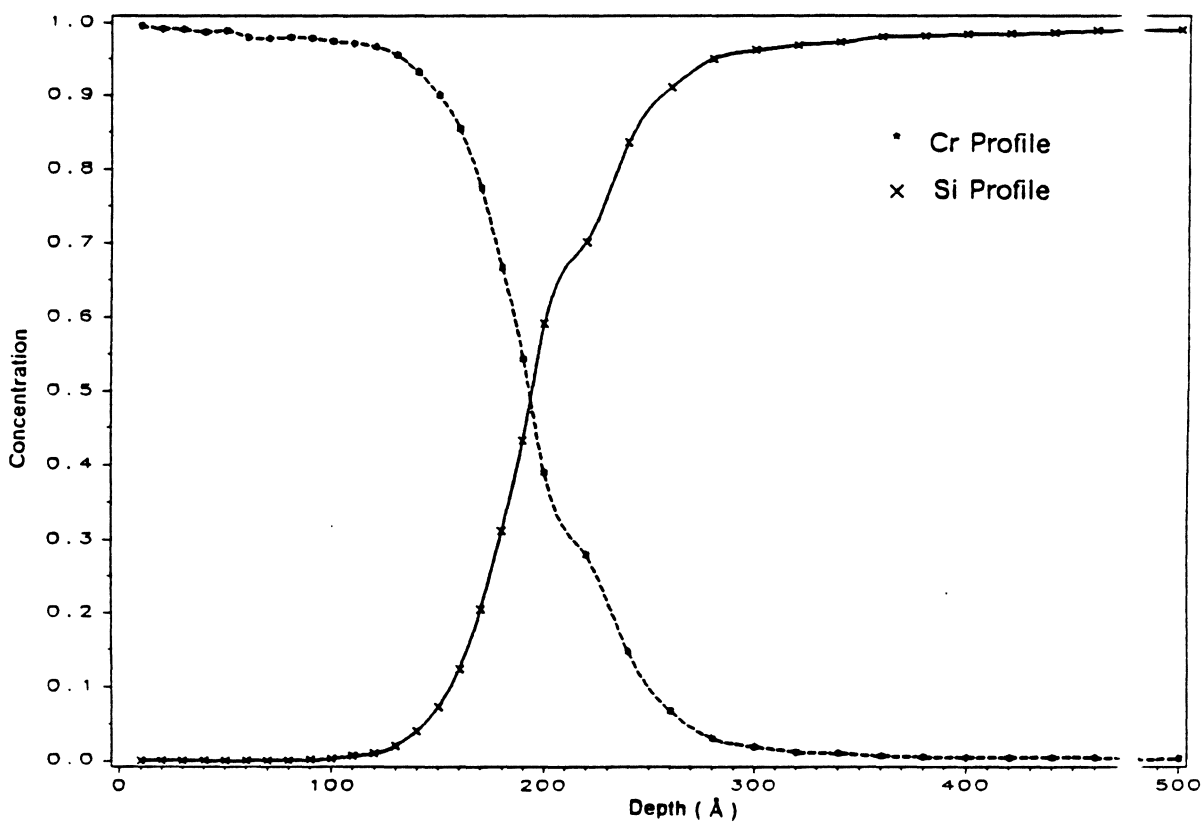

Figure 26. The composition profile of bilayer system Cr/Si implanted with 45 KeV Cr. This is the plot predicted by the computer code TRALL for dose of $0.6 \times 10^{16}/cm^2$. The experiment is from ref. [37].

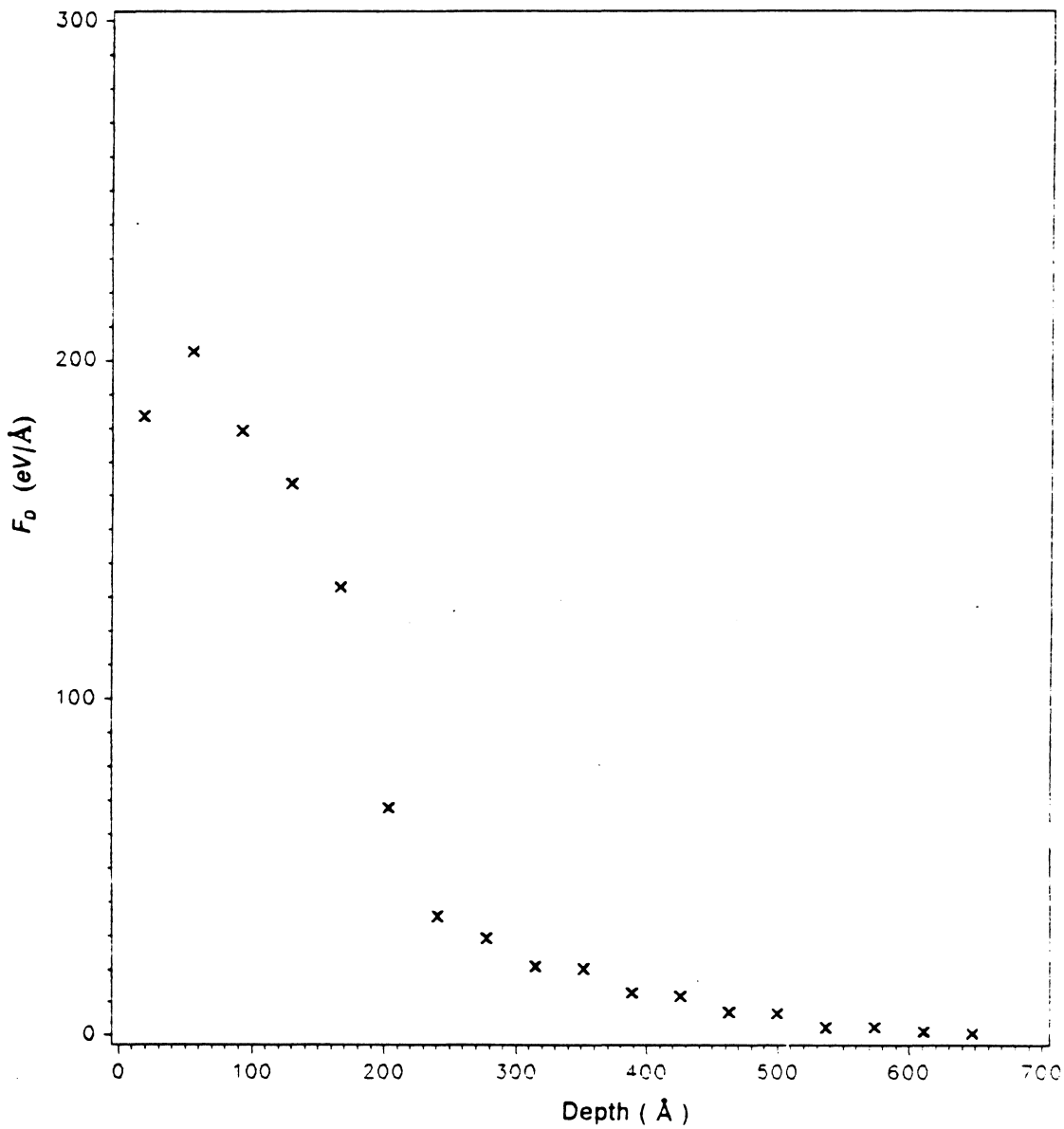

Figure 27. The damage energy profile for Cr/Si implanted with 45 KeV Cr. This is the plot predicted by the computer code TRIM. The Cr film thichness is 200 Å See ref. [37].

5.0 Discussion

5.1 Mo/Al Bilayer System

In the case of heavy-bombardment, it is well known that the collisional mechanism always underestimates the ion beam mixing results. For the ion mixing of Mo-Al system here, the atomic transport was dominated by thermal spike mechanism. In figure 15 the effective diffusion coefficient $D_T t$ was plotted as a function of doses. The linear relationship exists, as demonstrated by the straight line. The mixing parameter was then found to be $L_T = \frac{D_T t}{\Phi} = 1.75 \times 10^4$ (Å^4). Here $D_T t$ was calculated by using the formula [37]

$$D_T t = \frac{1}{2}\left(\frac{A}{N_0}\right)^2 \qquad (5-1)$$

where

$A = A_{Mo} + A_{Al}$.

$A_{Mo} = C_{Mo} - C^0_{Mo}$.

C_{Mo} and C^0_{Mo} are concentration integral in the concentration range of 0.95 to 0.05 for the irradiated samples and as-deposited samples respectively.

$A_{Al} = C_{Al} - C^0_{Al}$.

C_{Al} and C^0_{Al} are concentration integral in the concentration range of 0.95 to 0.05 for the irradiated samples and as-deposited samples respectively.

N_0 is the atomic density.

It should be noticed that in figure 15 the interdiffusion for the smallest dose point, $1 \times 10^{15}/cm^2$, was less than the linearly fitted curve. This phenomenon might be due to the fact that the Al oxide acted as a barrier at the interface of Mo/Al, protecting both Mo atoms and Al atoms from migrating through. However, for the higher doses these phenomenon no longer existed.

In figure 21, the Mo/Al bilayer mixing point was collected, as shown by the star point. The atomic density used $\rho = 0.06215 Å^{-3}$. The damage line density obtained from the TRIM F_D is 407.1 eV/Å. The relevant chemical parameters are: the heat of mixing $\Delta H_m = -24.3$ Kcal/mol, the cohesive energy

$$\Delta H_{coh} = \frac{1}{2}\Delta H_{coh}(Al) + \frac{1}{2}\Delta H_{coh}(Al) + \Delta H_m = -6.16 eV/atom$$

Eventually the Mo/Al bilayer mixing data showed very good correlation with the model developed in Chapter 4, as shown in figure 21.

5.2 *Thermal Spike Shapes*

The experimental data from references [15,17] were used to make a comparison with the model suggested in this Chapter 4. Table 12 lists the data in which the bilayer system has small chemical effect (with $-\Delta H_m \leq 31$ $kJ/g.at$). The data point Au/Co has been subtracted the chemical driving force induced diffusion. The plot of $\ln(4L_T\rho^{5/3})$ with $\ln \chi$ is shown in figure 19. The least square fitting in the abscissa range of 4.0 to 4.7 is given in the

plot. The slope is 2.24. So we take, $\mu = 0.33$, which follows the spherical spike model. For $\ln \chi \geq 4.8$, the data were not used for the fitting since they showed a much rapid increase of mixing thereafter. This prompts us the possible existence of another mixing mechanism behind what had been considered. We attribute this to the point defect density formula adopted here, i.e., the Kinchin-Pease formula. This formula is good only for the case of relatively high density cascade regions in which thermal spike related defects do not play an important role. When the characterization parameter χ reaches certain value, the spike related point defects can dominate the random walking in the spike region. In figure 19 at the first stage ($0 < \ln \chi \leq 4.7$) the defects random jumping in the spike region is attributable to the point defects created by collisional cascade; at the second stage ($\ln \chi > 4.7$) the defects random jumping is dominated by the spike related point defects. A formulation is suggested here. At low temperatures after the collisional cascade process ended, there are many agitated atoms in the spike region. Though they do not possess enough energy (their energy is less than the displacement energy) to knock down another atom, they can still have short term movement in the high cascade region and give out some of their energy to their neighbor atoms so that most of the atoms in the spike region becomes equalized energetically. In this energetic equalizing process, some of atoms absorb large amount of energy from more than two of their neighbor atoms by chance, and jump out of their regular position to become point defects. Thus in the liquid-like spike region a lot of additional defects are created by the collective atomic interaction, especially for the extremely high density cascade regions (i.e., high χ). Since the above calculated number of jumps per unit spike length (η_c) is equal to the number of point defects per unit length (n_c) times the number of jumps for each defect per unit time. So for the cylindrical spike model the spike related point defects number per unit length n_c can be deduced from equation (4-6)

$$n_c = p_c\left(-\frac{F_D}{\Delta H_{coh}}\right)^3 \qquad (5-2)$$

where p_c is a constant. After some manipulation as before the mixing parameter appears as

$$4L_T^{ch} = p'_c(-\frac{F_D}{\Delta H_{coh}})^5 \qquad (5-3)$$

where p'_c is a constant similar to B_1. Similarly, for the spherical spike model

$$n_s = p_s(-\frac{F_D}{\Delta H_{coh}})^{7/3} \qquad (5-4)$$

and

$$4L_T^{sh} = p'_s(-\frac{F_D}{\Delta H_{coh}})^{11/3} \qquad (5-5)$$

where p'_s is a constant similar to G_1

The second stage in Figure 17 corresponds to the case when the spike related point defects play an important role. The cylindrical spike model and spherical model are plotted respectively in the position of the best fit. The good fitting of the cylindrical spike model with the experimental data revealed that the cylindrical spike model dominates the second stage. In another word the spike is shaped like a cylinder in the extremely high density cascade regions.

In the Figure 18 the plot of $4L_T\rho^{5/3}F_D^{-4/3}$ with F_D was given in order to demonstrate the possible data fitting of the nonlinear effects caused by spikes. The least square fitting line is close to the spherical spike model. The data come from reference [6] in which the marker layer sample Pd(200Å)/Pt(5Å)/Pd were irradiated by different ions with certain kinetic energy. The data were listed in Table 13. The ballistic mixing efficiency was obtained to be 7.0 $Å^2/eV$ by the computer code TRALL [27] which was modified from the computer code TRIM. Nonlinear effect of mixing efficiency clearly exists and is beyond what can be explained by ballistic mixing model. The spike related point defects may have already played an important role for the data point Xe and Sm in figure 20.

5.3 Migration Mechanisms in the Spike Regions

Table 14 is the data from references [15,17]. Figure 19 is the plot of $4L_T\rho^{5/3}(-\frac{F_D}{\Delta H_{coh}})^{2.33}$ with $\Delta H_m/\Delta H_{coh}$, which follows the spherical spike model. The reason to use the spherical spike here is because more than eighty percent of the data used here follow the spherical spike. The deviation of the data point Au/Ag, Au/Co, Au/Cr from the fitting line is due to the effects caused by the spike related point defects in the extremely high density cascade regions as discussed above. The four data points around $\Delta H_m/\Delta H_{coh} = 0.08$ obviously deviated the general trend, so they were omitted in the least square fitting in figure 21. Finally, the results gave $G_1 = 0.29 \times 10^{-2}$ $Å^{4/3}$, and $J_s = 22.7$.

Substitute this result into equation (4-30), it was then found $Q = -\frac{1}{8.6}\Delta H_{coh}$. It is noticed that in the traditional annealing experiment the thermal activation energy of vacancy diffusion mechanism is approximately the same as the cohesive energy for metallic samples. Some people have conducted both ion beam mixing and thermal annealing work in metal-semiconductor bilayer samples and metallic samples, and found out that the activation energy in the ion beam mixing experiment was reduced by a factor of three to fifteen compared with thermal annealing[37,54,55,56,57]. These experimental results are consistent with the semi-empirical analyzing here. Furthermore, in our previous assumption of equations (4-1) and (4-2), two diffusion mechanisms were considered: vacancy mechanism and interstitial mechanism, and either of them dominates the atomic migration process in the spike regions. It is obvious that vacancy mechanism could be eliminated by the result of reduction in migration energy. Thus it is concluded that the interstitial mechanism dominates the atomic migration in the spike regions, and the atomic migration energy induced by spikes is equal to one out of 8.6 of the cohesive energy. This phenomenon might lie on two facts. One is the existence of high density of point defects in the cascade regions, the number of defects can be more than ten percent of atoms in that regions, much higher than the traditional number of defects (10^{-4}) of thermal annealing process. The other fact is because of the character-

istics of thermal spike, in which the equivalent temperature is so high (ten thousand K) and the region so localized.

The data of Mo/Al bilayer mixing is a little below the fitting line. Its interstitial migration energy is estimated about one out of 7.7 of its cohesive energy.

6.0 Conclusions

From the work developed above it can be concluded that

(i) Thermal spike is shaped like sphere in the relatively high density cascade regions, characterized by the line density parameter χ. For the metallic bilayer samples used in the above discussions, $\chi \leq e^{4.7}$, is the turning point in our data analyses. Then the formula obtained is

$$\frac{4D_T^s t}{\Phi} = 1.05 \times 10^{-2} \rho^{-5/3} \left(- \frac{F_D}{\Delta H_{coh}} \right)^{2.33} \qquad (6-1)$$

But in the extremely high-density cascade case, i.e., $\chi > e^{4.7}$, in the above data which we analyzed, the cylindrical spike gave better fit. The obtained formula for this region is

$$\frac{4D_T^{ch} t}{\Phi} = 3.4 \times 10^{-8} \rho^{-5/3} \left(- \frac{F_D}{\Delta H_{coh}} \right)^{5} \qquad (6-2)$$

(ii) The chemical effects has a significant influence on the whole mixing. The formula obtained is

$$\frac{4\tilde{D}_T^s t}{\Phi} = 0.97 \times 10^{-2} \rho^{-5/3} \left(- \frac{F_D}{\Delta H_{coh}} \right)^{2.33} \left(1 + 22.7 \frac{\Delta H_m}{\Delta H_{coh}} \right) \qquad (6-3)$$

and the thermally activated migration energy can be scaled by a factor of one out of 8.6 of the cohesive energy, that is,

$$Q = - \frac{1}{8.6} \Delta H_{coh} \qquad (6-4)$$

Clearly, there is good consistency in the coefficients between the equation (6-1) and equation (6-3).

(iii) The Kinchin-Pease formulation does not hold in the case of the extremely high dense cascade region since the spike related point defects also come to play an important role.

(iv) Due to the collective interaction in the high dense cascade region the nonlinear effect, as the power factor $(2 + \mu)$ determined above, obviously exists in the atomic random walking process, and is beyond what the ballistic mixing can account for.

(v) In the case of heavy-bombardment the interdiffusion of a metallic bilayer sample Mo/Al correlates the equation (6-3) very well. The atomic migration energy was reduced by a factor of 7.7.

(vi) The atomic migration mechanism in the spike region is an interstitial-dominated one, at least for metallic systems and metal-semiconductor systems.

(vii) The short-term partial annealing of point defects in the spike region was suggested to exist in some special cases, when the dimensionless parameter H_c for cylindrical spike or H_s for the spherical spike is close to one.

7.0 Further Work

1. Inert gas atoms are usually used as ion mixing source in ion beam mixing technique. The inert gas atoms should be rejected from the target materials and come out of the materials in the common sense, since their electronics structure does not keep them binding together with the target atoms favorably. In reality, however, the inert gas atoms were found inside the target materials, especially in the case of high dose irradiations. This arises the problem of how to evaluate the additional effect produced by the existence of a small amount of the inert gas. Based on the previous work and the work pioneered by Drs. Rao and Houska, it was suggested here to characterize the existence of Xe atoms inside the samples of Mo(3000Å)/Si(substrate), or Nb(3000Å)/Si(substrate), or Si substrate after being subjected to Xe irradiation with dose of $\simeq 1 \times 10^{16}/cm^2$, $4 \times 10^{16}/cm^2$, $7 \times 10^{16}/cm^2$, $10 \times 10^{16}/cm^2$. RBS can achieve the accurate Xe composition profile under the condition of different doses of irradiation. The x-ray technique may find out the form of Xe atoms as a point defect inside the target materials at two characteristic temperatures, liquid-nitrogen temperature and room temperature.

The accuracy of RBS analyses can be trusted except the top layer of thickness $\simeq$100Å due to the possible contamination of carbon's picking up. The x-ray technique may

be very reliable depending on the fabrication conditions of the samples. The single crystal films and substrate are preferred.

2. The model and the semi-empirical formulation were testified with the metallic bilayer systems. Further experimental work is needed to extend the system possibly to metal-semiconductor bilayer systems. Different regions of high density cascade are of high possibility to exist, which may be similar to the metallic systems. This investigation may provide more information of the cascade damage-induced effects as well as the nonlinear dependence of ion beam mixing on the parameter χ.

3. The inverse-Kirkendall effect during ion beam mixing is of great interest to the author. Further investigation is needed both experimental and theoretical. The author thinks that this effect may be related to the coupling of atomic migration induced by thermal spike with the chemically-biased walking. To solve this problem lies on two important facts. One is the determination of instantaneous distribution of point defects after spontaneous recombination of very near (about the length of the Frenkle pair) point defects following the collisional cascade. The other is the characterization of preferred jumping process of certain atoms in the matrices material into vacancies created by the collisional cascade. Twin marker experiments is hopeful to provide more quantitative information of the inverse-Kirkendall effect initiated by ion beam mixing.

8.0 BIBLIOGRAPHY

1. R. S. Averback, Nucl. Instr. & Meth. B15 (1986) 675-687.

2. W. L. Johnson, Y. T. Cheng, M. Van Rossum and M-A. Nicolet, Nucl. Instr. & Meth. B7/8 (1985) 657-665.

3. B. M. Paine and R. S. Averback, Nucl. Instr. & Meth. B7/8 (1985) 666-675.

4. P. Sigmund and A. Gras-Marti, Nucl. Instr. & Meth. 182/183 (1981) 25-41.

5. S.-J. Kim, B. M. Paine, M-A. Nicolet and R. S. Averback, Mat. Res. Soc. Symp. Proc. Vol.54, (1986) 723-730.

6. I. A. Fenn-Tye and A. D. Marwick, Nucl. Instr. & Meth. B18 (1987) 236-242.

7. J. Bottiger, S. K. Nielsen and P. T. Thorsen, Nucl. Instr. & Meth. B7/8 (1985) 707-710.

8. H. H.Andersen and H. L. Bay, J. Appl. Phys. 46, No. 6, 1975, p.2416.

9. D. A. Thompson and R. S. Walker, Rad. Effects, 36, 1978, p.91-100.

10. S.-J. Kim, M-A. Nicolet and R. S. Averback, Nucl. Instr. & Meth. B19/20 (1987) p.662-668.

11. A. J. Barcz and M-A. Nicolet, Appl. Phys. A33, 1984, p.167-173.

12. M. Rangswamy, Private discussions.

13. D. Farkas, I. L. Singer, and M. Rangaswamy, J. Appl. Phys. Vol 57, No. 15, 1985, p.1114-1120.

14. Y. T. Cheng, T. W. Workman, M-A. Nicolet and W. L. Johnson, Mat. Res. Soc. Symp. Proc. Vol 74, 1987, p.419.

15. M. Van Rossum, Y-T. Cheng, M-A. Nicolet and W. L. Johnson, Appl. Phys. Lett. 46 (6), 1985, p.610.

16. Y-T. Cheng, M. Van Rossum, M-A. Nicolet and W. L. Johnson, Appl. Phys. Lett. 45 (2), 1984, p.185.

17. T. W. Workman, Y. T. Cheng, W. L. Johnson and M-A. Nicolet, Appl. Phys. Lett. 50 (21), 1987, p.1485.

18. A. R. Miedema, Phili. Tech. Rev. Vol.36, 1976, No.8, P.217.

19. Kittel, Introduction to Solid State Physics, 5th edition, 1976.

20. K. Tao, C. A. Hewett, S. S. Lau, Ch. Buchal and D. B. Poker, Nucl. Instr. & Meth. B19/20, (1987) p.753-757.

21. L. S. Hung, E. G. Colgan and J. W. Mayer, Nucl. Instr. & Meth. B19/20, 1987, p.654-658.

22. Satish I. Rao, C. R. Houska, K. S. Grabowski, and G. Linker, Nucl. Instr. & Meth. B27 (1987) p.396-401.

23. Satish I. Rao, C. R. Houska and K. S. Grabowski, Nucl. Instr. & Meth. B18 (1986) p.47-53.

24. J. P. Biersack and L. G. Haggmark, Nucl. Instr. & Meth. 174 (1980) 257-269.

25. Wayne E. King and R. Benedek, J. Nucl. Mater. 117 (1983), p.26-35.

26. M. W. Guiman and J. H. Kinney, J. Nucl. Mater. (1981) p.1319-1324.

27. R. C. Pasianot, M. Rangaswamy, Diana. Farkas and Savino. Eduardo, to be published.

28. David Peak and R. S. Averback, Nucl. Instr. & Meth. B7/8 (1985) p. 561-565.

29. K. B. Winterbon, Ion Implantation Range and Energy Deposition Distributions, Vol 2 (Plenum, New York, 1975).

30. J. F. Ziegler, J. P. Biersack and U. Littmark, the Stopping and Range of Ion in Solids, Vol.1, 1985, p.115-116.

31. F. Seity and J. S. Koehler, Solid State Physics, Vol 2, p.251, (1956).

32. G. H. Vineyard, Radiation Effects, 1976, Vol.29, p.245-248.

33. H. L. Heinisch, J. Nucl. Mater. 103/104 (1981) p.1325-1330.

34. H. H. Andersen, Appl. Phys. 18, p.131-140 (1979).

35. P. Sigmund, Appl. Phys. A30, p.43-46 (1983).

36. S. Matteson, J. Roth and M-A. Nicolet, Radiation Effects, Vol 42, (1979), p.217.

37. S. Wen-Zhi Li, H. Kheyrandish, Z. Al-Tamimi and W. A. Grant, Nucl. Instr. & Meth. B19/20 (1987) p.723-730.

38. Y. T. Cheng, M-A. Nicolet and W. L. Johnson, Physical Review Lett, Vol. 58, 1987, p.2083.

39. G. J. Clark, A. D. Marwick and D. B. Poker, Nucl. Instr.& Meth. 209/210 (1983) p.107-114.

40. Lawrence R. Doolittle, Nucl. Instr. & Meth. B9 (1985), p344-351.

41. Lawrence R. Doolittle, Nucl. Instr. & Meth. B15 (1986), p.227-231.

42. Wei-Kan Chu, James W. Mayer and Marc-A. Nicolet, Backscattering Spectrometry, Academic Press, 1978.

43. B. Y. Tsaur, S. S. Lau, L. S. Hung and J. W. Mayer, Nucl. Instr. & Meth. 182/183. (1981) p.67-77.

44. B. M. Paine, J. Appl. Phys. 53(10), 1982, P.6826.

45. S. Matteson, B. M. Paine, M. G. Grimaldi, G. Mezey, and M-A. Nicolet, Nucl. Instr. & Meth. 182/183. (1981) p.43-51.

46. S. Matteson, B. M. Paine, and M-A. Nicolet, Nucl. Instr. & Meth. 182/183. (1981) p.53-61.

47. C. S. Pai, S. S. Lau, D. B. Poker and L. S. Hung, J. Appl. Phys., Vol.58 (11), 1985, p.4172.

48. C. S. Pai, S. S. Lau, D. B. Poker and L. S. Hung, J. Appl. Phys., Vol.58 (11), 1985, p.4178.

49. Jr Frank V. Nolfi, Phase Transformations During Irradiation, Applied Science Publications, 1983.

50. P. H. Dederichs, R. Zeller, and K. Schroeder, Point Defects in Metals Vol.2, Springer-Verlag Berlin Heidelberg New York 1980.

51. Orlando Auciello and Roger Kelly, Ion Bombardment Modification of Surfaces, Elsevier, Amsterdam-Oxford-New York-Tokyo, 1984.

52. S.-J. Kim, M-A. Nicolet, R. S. Averback and D. Peak, to be published.

53. S.-J. Kim, D. N. Jamieson, M-A. Nicolet and R. S. Averback, to be published.

54. J. W. Mayer, B. Y. Tauser, S. S. Lau and L. S. Hung, Nucl. Instr. and Meth. 182/183 (1981) p.1.

55. R. S. Averback, L. J. Thompson Jr., J. Moyle and M. Shailt, J. Appl. Phys. Vol 53, (1982) p. 1342.

56. S. S. Lau, J. W. Mayer and K. N. Tu, J. Appl. Phys. Vol 49, (1979) p.4005.

57. S. Matteson, J. Roth and M. A. Nicolet, Radiat. Eff. Vol 42, (1979) p.3978.

Appendix A. The Important Mathematics Symbols Used in the Thesis

A = the temperature-independent constant assumed by Vineyard's model[32]. See page 9.

c = the specific heat of the target material.

D_b = the effective general diffusion coefficiency in ion beam mixing.

$D_b t$ = the effective diffusion coefficiency related to collisional mixing.

$D_T t$ = the effective diffusion coefficiency related to thermal spike induced diffusion.

$D_T^c t$ = the effective diffusion coefficiency related to cylindrical spike induced diffusion.

$D_T^s t$ = the effective diffusion coefficiency related to spherical spike induced diffusion.

$\tilde{D}_T^c t$ = the effective diffusion coefficiency related to the coupling of chemical effect with cylindrical spike.

$\tilde{D}_T^s t$ = the effective diffusion coefficiency related to the coupling of chemical effect with spherical spike.

$D_T^{ch} t$ = the effective diffusion coefficiency related to cylindrical spike in the extremely high density cascade regions.

$D_T^{sh}t$ = the effective diffusion coefficiency related to spherical spike in the extremely high density cascade regions.

E_d = the atomic displacement energy.

E_D = the damage energy.

F_D = the damage energy deposited per unit pass length.

H_c = the parameter characterizing the short-term annealing process for the cylindrical spike.

H_s = the parameter characterizing the short-term annealing

$L \equiv \frac{Dt}{\Phi}$ = the general mixing parameter in ion beam mixng.

$L_A^c \equiv \frac{D_A^c t}{\Phi}$ = the mixing parameter related to the short-term partial annealing of the point defects in the cascade regions with cylindrical spike.

$L_A^s \equiv \frac{D_A^s t}{\Phi}$ = the mixing parameter related to the short-term partial annealing of the point defects for spherical spike.

$L_b \equiv \frac{D_b t}{\Phi}$ = the mixing parameter related to ballistic mixing in the collisional processes.

$L_T \equiv \frac{D_T t}{\Phi}$ = the mixing parameter induced by thermal spikes.

$L_T^c \equiv \frac{D_T^c t}{\Phi}$ = the mixing parameter related to the cylindrical spike-induced atomic transport in the relative high density cascade regions.

$L_T^s \equiv \frac{D_T^s t}{\Phi}$ = the mixing parameter related to the spherical spike-induced atomic transport in the relative high density cascade regions.

$L_T^{ch} \equiv \frac{D_T^{ch} t}{\Phi}$ = the mixing parameter related to the cylindrical spike-induced atomic transport in the extremely high density cascade regions.

$L_T^{sh} \equiv \frac{D_T^{sh} t}{\Phi}$ = the mixing parameter related to the spherical spike-induced atomic transport in the extremely high density cascade regions.

$\tilde{L}_T^c \equiv \frac{\tilde{D}_T^c t}{\Phi}$ = the mixing parameter related to the cylindrical spike-induced atomic transport in the extremely high density cascade regions.

$\tilde{L}_T^s \equiv \frac{\tilde{D}_T^s t}{\Phi}$ = the mixing parameter related to the spherical spike-induced atomic transport in the extremely high density cascade regions.

N = the number of point defects predicted by Kinchin-Pease formula.

n_0 = the line density of point defects in the extremely high density cascade regions.

Q = the migration energy of point defects.

$Q_0 \equiv \frac{Dt}{\Phi F_D}$ = the general ion beam mixing efficiency.

$Q_b \equiv \frac{D_b t}{\Phi F_D}$ = the ion beam mixing efficiency caused by collisional mixing.

$Q_T \equiv \frac{D_T t}{\Phi F_D}$ = the ion beam mixing efficiency induced by thermal spikes.

r_1 = the root-mean square jumping distance relevant to spike-induced atomic migration.

r_c = the root-mean square jumping distance relevant to the ballistic mixing process.

α = the jumping frequency of point defects cross unit section in the spike regions.

χ = $-F_D/\Delta H_{coh}$, which characterizes the line density of point defects in the cascade regions.

ΔH_{coh} = the cohesive energy, that is, the difference between free atom energy and crystal energy.

ΔH_m = the heat of mixing.

η_c = the total number of jumps of point defects induced in one spike per unit length of the cylindrical spike.

η_s = the total number of jumps of point defects induced in one spike per unit length of the spherical spike.

$\tilde{\eta}_c$ = the total number of jumps of point defects induced in one spike per unit length of the cylindrical spike, coupled with chemical effects.

$\tilde{\eta}_s$ = the total number of jumps of point defects induced in one spike per unit length of the spherical spike, coupled with chemical effects.

Γ_c = the jumps per unit volume per unit time related to cylindrical model.

Γ_s = the jumps per unit volume per unit time related to spherical model.

$\tilde{\Gamma}_c$ = the jumps per unit volume per unit time related to cylindrical model and enhanced by chemical effects.

$\tilde{\Gamma}_s$ = the jumps per unit volume per unit time related to spherical model and enhanced by chemical effects.

κ = the heat conduction coefficient.

λ = the dimension of a single cascade.

μ = the power factor. See page 66.

Φ = the dose of incident ions.

ρ = the atomic density.

τ = the lifetime of point defects.

The vita has been removed
from the scanned document